Plasmonic Ag-Pd core-cluster catalyst for selective oxidation reaction

Ziqi Zhou

BSc (Chem)

Submitted in fulfilment of the requirements for the degree of
Master of Philosophy (Science)

Centre for Materials Science
School of Chemistry and Physics
Faculty of Science
Queensland University of Technology

2022

Keywords

Photocatalysis; Metal NP; biomass; 2,5-Furandicarboxylic acid.

Abstract

Since photocatalysis utilizes solar energy, it has tremendous potential for various applications. Solar light's abundant availability and cleanliness as a renewable energy source have received considerable attention for synthesizing fine chemicals at ambient temperatures. Therefore, it is highly desirable to synthesize fine chemicals using solar light at ambient temperatures. Despite this, it remains challenging to devise new catalysts that perform well under all solar spectrum conditions and moderate temperatures. This project investigates a significant organic reaction using novel metal NPs as photocatalysts to apply visible light. As a result of irradiating chemical synthesis with visible light, the scope of organic synthesis may be significantly enhanced through a more accessible, more straightforward, and greener process.

As fossil fuel consumption and their chemical products increase rapidly, new energy sources are being explored at an increasing rate. The modern energy revolution has relied heavily on biomass for fuel and chemicals as a cheap renewable energy resource. Several valuable products can be extracted from the plant, including 5-hydroxymethylfurfural (HMF), 2,5-diformylfuran (DFF), 5-hydroxymethyl-2-furancarboxylic acid (HMFCA), and 2,5-furandicarboxylic acid (FDCA). Among these derived products, 2,5-furandicarboxylic acid (FDCA), an excellent precursor for producing green polymers, has been an excellent precursor, such as 2,5-furandicarboxylate (PEF) excellent precursor received considerable attention recently. Most methods require harsh conditions to oxidize HMF to FDCA, including high pressures and temperatures and environmentally unfriendly reactants. Therefore, it has been challenging to find an economical and green technique to synthesize FDCA.

This study demonstrated a ceria-supported Ag@Pd photocatalytic system to achieve the FDCA transformation under ambient conditions. This system achieved excellent yields (over 90 per cent) of FDCA within 4 hours under green light irradiation. A major benefit of this system is that the amount of palladium required is relatively low. These findings provided an excellent foundation for developing green synthesis from biomass-derived products powered by solar energy.

Table of Contents

List of Figures

List of Tables

List of Abbreviations

NPs	Nanoparticle
LSPR	Localized surface plasmon resonance
HOMO	Highest occupied molecular orbital
LUMO	Lowest unoccupied molecular orbital
TON	Turnover number
HMF	5-hydroxymethylfurfural
HMFCA	5-Hydroxymethyl-2-furancarboxylic acid
FFCA	5-Formyl-2-furancarboxylic Acid
FDCA	2,5-Furandicarboxylic acid
WI	Wet impregnation
DI	Dry impregnation
IWI	Incipient wetness impregnation
UV	Ultraviolet
UV-Vis	Ultraviolet-visible spectroscopy
HPLC	High performance liquid chromatography
TEM	Transmission electron microscope
SEM	Scanning electron microscope
XRD	X-ray diffraction
AQE	Apparent quantum efficiency
EDS	Energy dispersive X-ray spectroscopy
XPS	X-ray photoelectron spectroscopy

Acknowledgements

I wish to express my deepest gratitude to my principal supervisor, Dr. Sarina Sarina, and my associate supervisors, Prof. John McMurtrie and A/Prof. Eric Waclawik, for their invaluable guidance, support, and encouragement during my master's work. I would like to thank Queensland University of Technology (QUT) for the Tuition Fee Sponsorship. I would also like to thank Dr. Sarina Sarina for the Supervisor Scholarship.

I am pleased to extend my appreciation to the E block and Central Analysis Research Facility staff. Mr. Peter Hegarty, Dr. Dilini Galpayage Dona, Ms. Rebecca Fieth, Dr. Jess Wu, Dr David Marshall, Dr. Tony Wang, Ms. Elizabeth Graham, and Dr. Aaron Micallef, who supported me in operating UV-Vis, NMR, TEM, SEM, EDS, XRD, XPS, and Mass spectrometry. It would be tough for this project to progress without their assistance.

Additionally, I wish to thank all the colleagues and friends who have supported and encouraged me throughout this journey.

Last but not least, I would like to thank my parents for their strong support and company during this lonely and difficult time. They provide me with solid backing so that I can pursue my dreams bravely.

Chapter 1: Introduction

This chapter outlines the background (section 1.1) and context (section 1.2) of the research. Finally, section 1.3 includes the purposed, significance and scope of the thesis.

1.1 BACKGROUND

Metal NPs (NP) have recently attracted considerable attention as photocatalysts. These catalysts enable organic reactions to be carried out at ambient temperatures and the by-products to be reduced at an extremely low level.[1] At the same time, the ease of separation and reuse makes heterogeneous catalysis more favourable than homogeneous catalysis. Recently, we found metal NPs strongly absorb visible light, which shows high activity for various organic reactions, such as Suzuki cross-coupling reactions,[2] hydroamination reactions,[3] nitrobenzene coupling reactions.[4]

Metal NPs could strongly absorb visible light due to the LSPR (LSPR) effect. This effect occurs when the conduction electrons resonate with the electromagnetic field of the incident light, which enables these electrons to absorb light irradiation energy and energize electrons on the metal NP surface. Then the reactants would be activated for further reactions. Besides, as LSPR is driven by ultraviolet-visible light, metal NP photocatalysts inspire more possible pathways for converting solar energy to chemical energy. There are many excellent example reactions catalyzed by supported monometallic,[5] bimetallic,[6] or trimetallic[7] NPs at ambient conditions.

1.2 CONTEXT

The worldwide consumption of fossil fuel and its chemical products is increasing swiftly,[8] which dramatically drives the exploration of new energy resources. As a cheap and renewable resource, biomass-derived fuels and chemicals play a vital role in the modern energy revolution.[9] Also, as a result of the high dependency on polymers in modern economics, several industries have begun considering using bio-based

chemicals for making bioplastics, such as polyethylene terephthalate, polyamides, and polyurethanes.[10] It is evident from Figure 1 that there are several routes for producing bioplastics starting from LCB. In most cases, the LCB molecules are turned into monomers using either chemical or biological techniques, followed by polymerization to make bio-based polymers. [11]

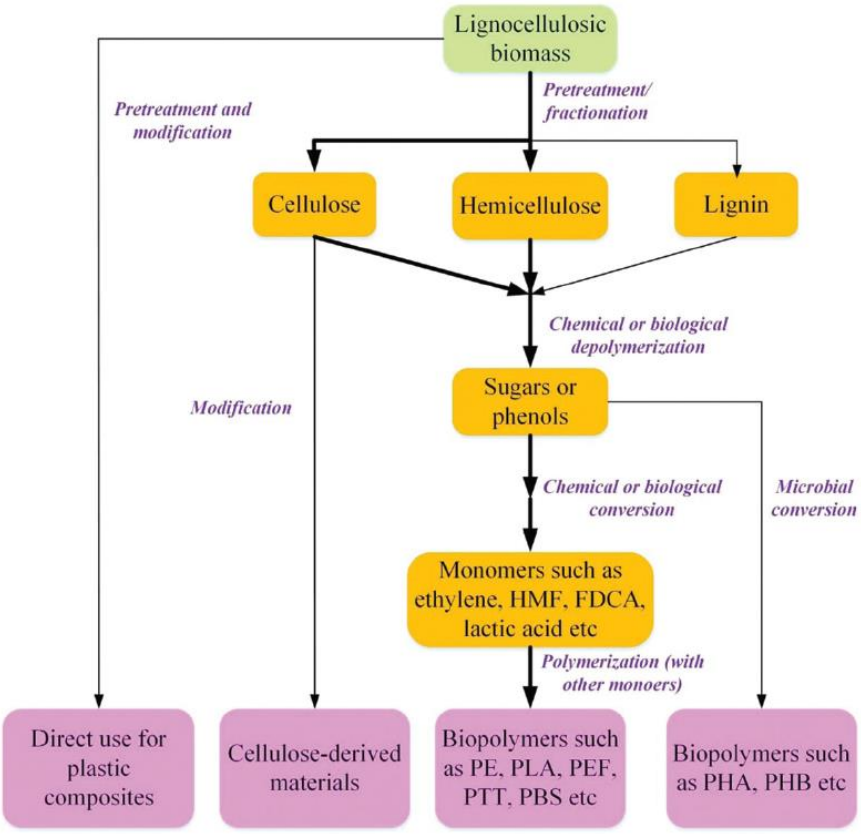

Figure 1 Typical production routes of bio-based polymers from lignocellulosic biomass. Reproduced with permission from ref.[10]

HMF is a degradation product of C6 carbohydrates and has abundant valuable products, such as 2,5-diformylfuran (DFF), 5-hydroxymethyl-2-furancarboxylic acid (HMFCA), and 2,5-furandicarboxylic acid (FDCA).[12] Among these products, FDCA is one of the most significant platform chemicals.[13] For instance, as a critical renewable building block, FDCA empowers the production of polyesters, polyamides, and polyurethanes.[14] One of the approaches to producing FDCA is the catalytic oxidation (Figure 2) of 5-hydroxymethylfurfural (HMF), which numerous pathways have investigated.[15, 16]

Recent studies have shown that alloy catalysts demonstrate dramatically different product selectivity than monometallic NP catalysts.[17, 18] Silver NPs were reported to catalyze the selective oxidation from HMF to HMFCA,[19] but cannot catalyze the alcohol side chain of HMFCA to aldehyde side and then the carboxyl of FDCA. Palladium NPs are widely loaded on different photocatalysts to conduct plasmonic photocatalysis on various organic reactions,[20, 21] and have been a more prior choice for chemical reactions due to their high activity, stability, and selectivity.[22] However, most research findings require high Pd loading to achieve great catalytic performance.[23, 24] Besides, palladium has become the most expensive metal nowadays with a dramatic increase in its price (almost $100 per g).[25] These findings and database inspired us to investigate diverse methodologies to integrate palladium of lower content with silver to obtain higher photoactivity on the oxidation of HMF to FDCA. Both Ag and Pd atoms have face-centered cubic crystal structures and extremely close sizes, making it possible to alter the reaction pathways by tuning the surface configuration of the metal NPs.

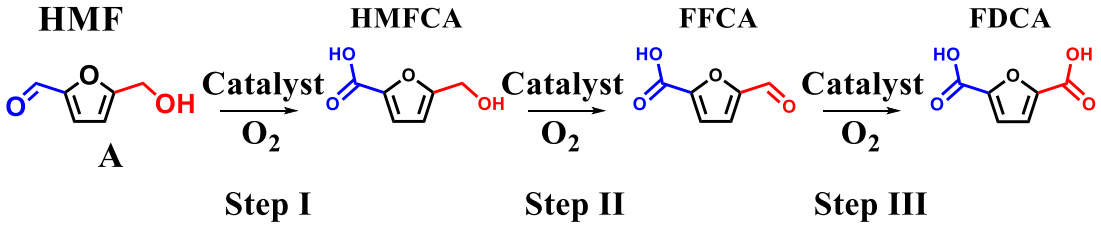

Figure 2. Reaction pathways for the catalytic oxidation of HMF to FDCA with molecular oxygen in water.

1.3 PURPOSES, SIGNIFICANCE AND SCOPE

This project aims to develop an eco-friendly and economical route to synthesize FDCA from HMF, which follows the four-stage experiments.

Stage 1: Synthesize cerium oxide and load metals on it.

Stage2: Find appropriate active metals and convert HMF into FDCA under light.

Stage 3: Optimize the reaction conditions to achieve high conversion rate and product selectivity by altering reactants, temperature, light intensity, light wavelength.

Stage 4: Investigate and explain how the organic transformations can be conducted on the surface of the photocatalysts.

In this study, $Ag_{2.5}@Pd_{0.5}/CeO_2$ was found to show excellent catalytic performance on HMF oxidation compared to the photocatalysts prepared by other methods, such as mechanical mixture and alloy NP. To the best of our knowledge, nobody has reported a photocatalyst with such lower palladium content that can exhibit excellent performance. Apart from that, unlike other catalysts that use the thermal effect to catalyze the HMF oxidation reaction,[26, 27] $Ag_{2.5}@Pd_{0.5}/CeO_2$ takes full advantage of light based on green chemistry while reducing the generation of by-products. This discovery may contribute to a new pathway to catalyze organic reactions and reduce the experimental cost. In addition, we will interpret the results in terms of the influence of surface configuration on its active sites and analyze the effect of nanostructures on its photocatalytic properties.

Chapter 2: Literature Review

2.1 DIRECT PHOTOCATALYSIS ON PLASMONIC-METAL NPS

Compared to those bulk materials, metal NPs have unique characteristics. For instance, due to the LSPR (LSPR) effect, silver and gold NPs are strongly capable of absorbing visible light. Its absorbance is significantly influenced by the size and shape of the metal NPs.[28] The utilization of LSPR to drive photocatalysis generally falls into two sorts: (a) direct photocatalysis, the metal NP itself absorbs the light and acts as the active sites,[29] and (b) indirect photocatalysis, the LSPR empowers the photon energy transfer from the metal NP to the nearby semiconductors,[30] or other metals.[31] Coinage metals like silver, gold, and copper act as both light absorbers and active catalyst sites,[29] herein focusing more on direct photocatalysis.

2.1.1 Localized Surface Plasmon Resonance (LSPR)

Plasmonic metal NPs are defined by their strong interaction with the incident light through LSPR. This effect occurs when the conduction electrons resonate with the electromagnetic field of the incident light (Figure 3), which will enable these electrons to absorb light irradiation energy and to energize electrons on the metal NP surface. Herein, metallic NPs such as Ag, Au, and Cu can absorb visible and infrared light in an extensive range of wavelength.[32]

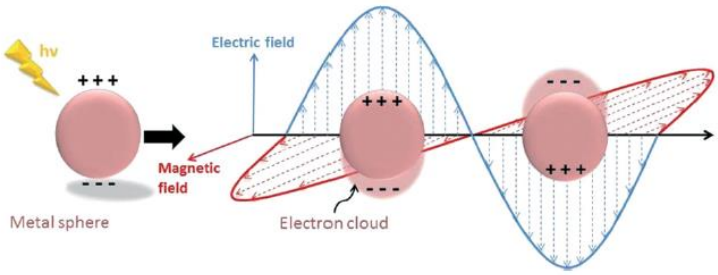

Figure 3 Schematic illustration of a LSPR. Reproduced with permission from ref.[1]

The modification of the composition, size, and morphology of the metal NPs could change their intrinsic metallic properties, atmospheric medium, or surface polarization, then influence the frequency and strength of the plasmon oscillation.[33]

The oscillating change will reflex on the light absorption. Below is an example of Ag NPs (Figure 4). When the particle shape changes from sphere to cube, there will be a plasmon absorption shift from 400-700 nm, and when the particles grow larger, the absorption band will broaden and shift to a longer wavelength.[34]

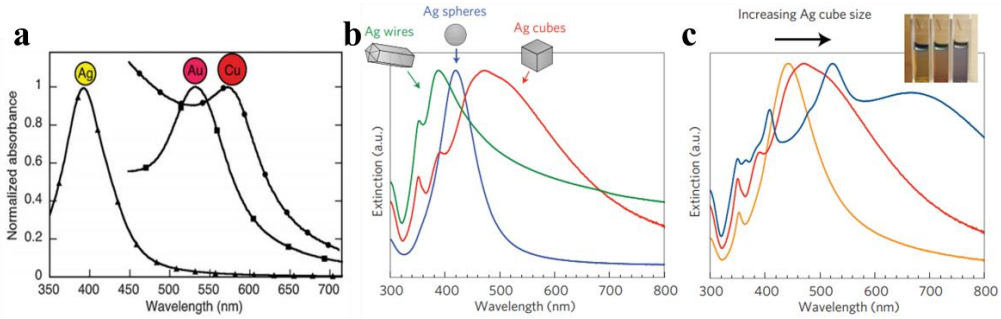

Figure 4 a) Surface plasmon absorption bands for Au, Ag, and Cu NPs. Reproduced with permission from ref.[32] b) Normalized extinction spectra for Ag wire, cube, and sphere NPs. c) Normalized extinction spectra for Ag nanocubes as a function of size; the inset shows a photograph of the three nanocube samples suspended in ethanol. Reproduced with permission from ref.[34]

Two processes, including light absorption and activation of the reactants, will occur on the metal NPs. These interactions can generate high concentrations of energetic electrons and a strong electric field on the metal surface. The light energy produced here can be transferred into the adsorbed reactants in direct plasmonic-metal photocatalysis through three pathways (depicted in Figure 5): (1) elastic radiative re-emission of photons, (2) non-radiative Landau damping (the excitation of energetic charge-carriers in the metal particle causes) and (3) the interaction of excited surface

plasmons with unpopulated adsorbate acceptor states, inducing direct electron injection into the adsorbate, which is called chemical interface damping.[35]

Additionally, due to the high concentrations of electrons on NP surfaces, chemical reactions may be caused because of the localized electric fields generated by light absorption. Based on the results obtained by comparing the reaction rates of plasmonic metals photocatalyzed at various wavelengths and intensities, it was clearly demonstrated that LSPR contributed significantly to the enhancement of photocatalytic reactions.[5] A correlation between the measured photocatalytic rate and the calculated plasmon absorption intensity was used to determine whether the

photocatalytic rate was plasmonically enhanced. According to the linear relationship between photoinduced rate and source intensity, an electron-driven chemical process is distinct from a traditional thermal heating process. The photoinduced rate is linearly correlated with the source intensity.[36] Depending on the intensity and wavelength of the light, it has been proposed that the LSPR is a significant contributor to photocatalytic activity.

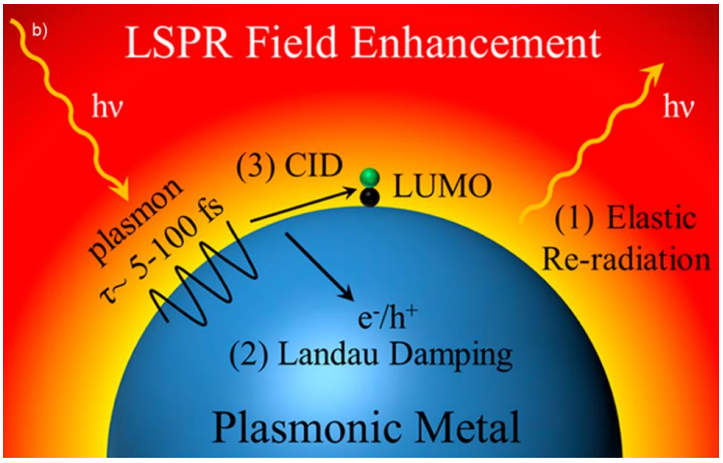

Figure 5 Schematic showing the three dephasing mechanisms of oscillating surface plasmons. Reproduced with permission from ref.[35]

The light-induced plasmons may generate energetic charge carriers to help shift the energy obtained from the irradiation, transfer the energetic electrons into the absorbents, and then facilitate chemical reactions.[37] Two possible pathways can drive this transformation indirect and direct.[38] For the indirect charge transfer mechanism, the absorbent acceptor orbitals have energies closer to Fermi level because the low-energy electrons are in a higher concentration. Therefore, the excited energetic charge carriers prefer to transfer the energy to these orbitals, the lowest unoccupied molecular orbital (LUMO). In the case of the direct charge transfer mechanism, plasmon-mediated charge scattering drives the transfer.[39]

The electromagnetic field generated by two or more metal NPs that are close enough together can be significantly stronger than the electromagnetic field generated by a single metal NP.[40] There are many areas between the NPs in which there are stronger electromagnetic fields. A finite-difference time-domain simulation of local plasmonic hot spots can result in an electric field intensity of up to 106 times more intense than the incident electric field.[41] Furthermore, the electron-hole pairs generation rate in hot-

spot areas of metal NPs is 1000 times higher than in incident electromagnetic fields. In addition to solvent and support materials, the surrounding environment influences metal NPs' LSPR absorption.

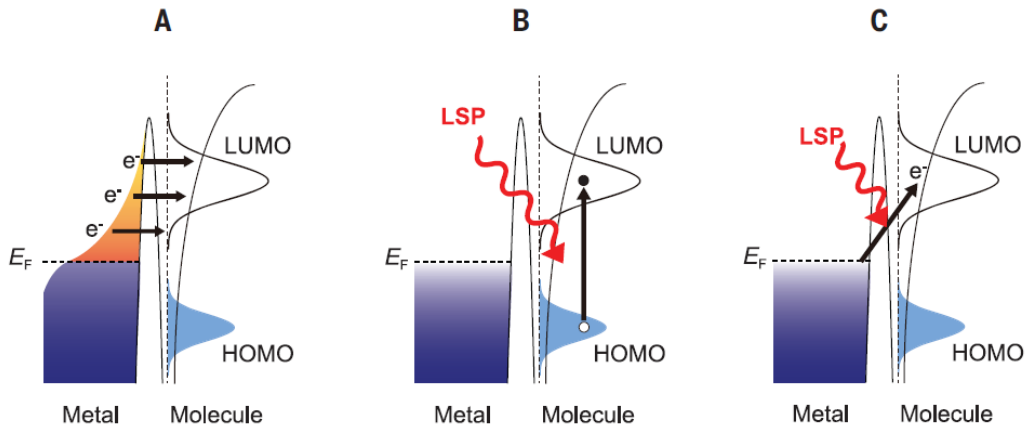

Figure 6 Excitation mechanisms for plasmon-induced chemical reactions. (A) Indirect hot-electron transfer mechanism. Hot electrons (e^-) generated via non-radiative decay of an LSP transferred to form the molecule's transient negative ion (TNI) states. (B) Direct intramolecular excitation mechanism. The LSP induces direct excitation from the occupied state to the unoccupied state of the adsorbate. (C) Charge transfer mechanism. The electrons are resonantly transferred from the metal to the molecule. Reproduced with permission from ref.[42]

2.1.2 The impact of supports

Although the metal NP can catalyze organic transformations, they are not stable under typical reaction conditions.[43] Therefore, in practical applications, most plasmonic metal NPs are supported on inert solid supports, such as metal oxides and carbon-based supports and porous materials. The selection of the support material may impact the reaction pathway without being just a substrate. For example, the light excited electrons can transfer to the metal oxide support to contribute to the reaction.[44] Cu NPs can be stable when supported on graphene rather than metal oxide supports.[45] The product selectivity may be affected by the porosity of the support.[46]

2.2 SUPPORTED METAL PHOTOCATALYSTS

The active components of the photocatalyst are metals, and only their surfaces are capable of catalyzing chemical reactions. Therefore, maximizing the area of the catalyst contacting with the reactants could develop catalytic efficiency. There are various thermally stable, high-surface-area materials (in nanoscale, typically below 10 nm) used as the supports, including alumina (Al_2O_3), silica (SiO_2), titania (TiO_2), carbon (C), ceria (CeO_2), etc. To synthesize metal NPs in controllable size has been the most significant challenge, and the preparation techniques incredibly affect the activity, selectivity, and lifetime of the photocatalyst.[47]

2.2.1 Preparation techniques

Among the various ways to prepare supported metal catalysts, impregnation is mainly chosen due to its simpleness and low waste. Impregnation is typically distinguished into two methods, wet impregnation (WI) and dry impregnation (DI), also termed incipient wetness impregnation (IWI).[48]

This method requires a metal precursor solution to contact the support fully. The most common precursors are metal salts, including metal sulfates, carbonates, and nitrates. Water is widely used as a solvent because of the high solubility of many precursors. Then strong reducing agents like sodium borohydride ($NaBH_4$) is used to generate metal NPs of smaller sizes (< 10 nm). Adding an amount of capping reagent such as lysine to be absorbed on the surface of supported metal NPs can avoid aggregation. In WI, the impregnated catalysts can be obtained by filtration, while the excess precursor solution would be reused to minimize the waste. In DI, some counterions from the precursor solution, such as platinum tetraamine chloride might retain in the dried catalyst without filtration, leading to contaminants.[49] To obtain fully reduced zero-valent metal NPs anchored on the support, different thermal treatments like calcination in a reducing (H_2 atmosphere) environment would be acceptable.

2.2.2 Applications of Metal NPs in Photocatalysis

2.2.2.1 Selective oxidation reactions

Alcohols are essential platform molecules for developing various value-added products in the fine chemical, pharmaceutical, and agrochemical sectors, including but not limited to aldehydes, ketones, ethers, etc.[50] In most studies, the oxidation of alcohol requires a longer reaction time, certain oxygen pressure, and the high temperature, generation of by-products, which cause many limitations. Therefore, developing a technique, which is selective oxidation of alcohol under ambient conditions, has become a challenge.

Here some cases utilizing energy from light to catalyze alcohol oxidation provide new hints in this field. Sarina and co-workers reported a highly efficient AuPd system catalyzing the oxidation of aromatic alcohols under light irradiation.[51] The reactions were conducted in trifluorotoluene at around 45^{o}C and under 1 atm of Ar after O_2 removal using freeze-pump-thaw degassing. For the dehydrogenation of benzyl alcohol, Au-Pd/ZrO_2 with a 1:1 Au:Pd mass ratio achieved a 100% conversion rate under visible light. By contrast, only 43% was obtained under dark conditions. Similar results were obtained for other alcohol reactants like 4-methoxybenzyl alcohol, 1-phenylethanol, etc. According to the experimental data, a tentative mechanism for this photocatalytic process was proposed in Figure 7. The rate-determining step of the aromatic alcohol oxidation was investigated to occur on the alloy NP surface. α-H atoms of the alcohol molecules are abstracted, followed by the subsequent abstraction of the hydrogen atom from the hydroxyl group. When the negative charge of the transient anions returns to the alloy, the final product aldehydes are generated. The LSPR effect drives the conduction electrons on the alloy NPs to gain energy from the incident visible light during this photocatalysis process. Due to the electron redistribution and electron-electron between Au and Pd, these energic electrons are active on the NP surface. Also, the good affinity of the Pd sites to the alcohols enhances

the interaction between the absorbed reactants and NP, then drive the chemical transformations.

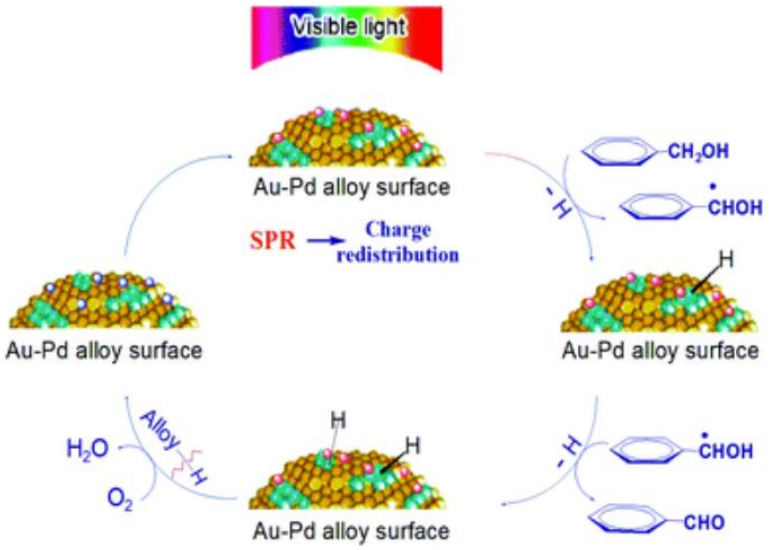

Figure 7 Proposed mechanism of aromatic alcohol oxidation over Au–Pd alloy NPs under visible light irradiation. Reproduced with permission from ref.[51]

Metal NPs photocatalysis has also played a significant role in other oxidation transformations. For example, Huang and co-workers reported a photocatalytic system Ni clusters supported on CdS to produce imines from amines by oxidation procedures, which achieved a dramatic apparent quantum efficiency of ~44% under 420 nm irradiation.[52] For ester derivative synthesis, Zhang *et al.* reported an alternative technique to convert aldehyde to esters in mild conditions based on Au NP photocatalysts.[53]

2.2.2.2 Selective reduction reactions

Reduction reactions have been intensely studied in organic synthesis and biological chemistry. Aromatic azo compounds can be applied in various fields, such as organic dyes, therapeutic agents, and intermediates for natural product production.[54] Traditional techniques of synthesizing azo compounds involve using toxic reactants or agents like nitrile salts, Nitrosobenzene intermediates, which do not accord with the green chemistry principle.[55] Mondal and co-workers reported a cage encapsulated gold NP involved in a photocatalysis process for the selective reductive nitroarene to azo

compounds.[56] This work utilizes sodium hydride in isopropanol under nitrogen, 30°C, and ultraviolet irradiation, obtaining a perfect conversion and selectivity of the target azo compound. Four proposed reaction routes have been hypothesized based on the ^{1}H NMR and ESI-HRMS analysis. Initially, sodium hydroxide drives the abstraction of a hydrogen atom from isopropanol, giving the intermediate isopropoxide. Then with the presence of UV light, hot electrons, and holes produced by Au NPs further generate AuNPs-H by capturing the hydride from sodium isopropoxide, giving the acetone as the product. After that, Au-H bond transfers hydrides to nitroarene to produce nitroso-arene by eliminating water. Finally, the nitroso-arene was assumed to be converted to azoarene via hydroxide transfer. Also, Peiris and co-workers discovered an AgPd alloy system to reductively couple nitrobenzene under visible light irradiation and ambient conditions, achieving a great conversion rate.[4] Figure 8 introduces a possible mechanism involving Ag-Pd-H species as an essential intermediate for generating azo compounds.

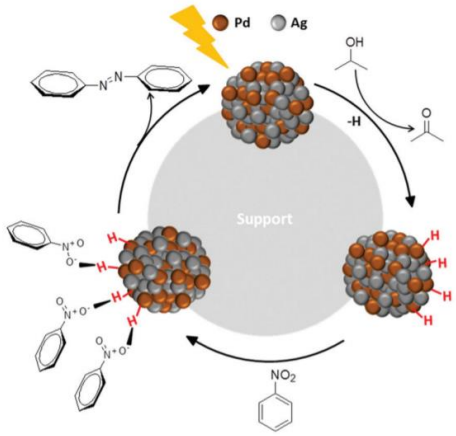

Figure 8 Proposed mechanism of reductive coupling of nitroaromatic compounds over Ag–Pd alloy NPs under visible light irradiation. Reproduced with permission from ref.[4]

Metal NPs have also been involved in diverse reduction reactions, like selective reduction of epoxides,[57] alkenes, and alkynes.[58] Where the generation of important intermediate like Metal-H, Metal-OH facilitates the reduction transformations.

2.2.2.3 Other reactions based on supported metal photocatalysts

Organometallic compounds mediated cross-coupling reactions have been applied to synthesize a variety of bonds, including C-C, C-O, C-N, C-S.[59] These transformations have been regarded as an appropriate technique for synthesizing natural [60] medicines[61] and advanced materials.[62] Among these reactions, some utilize metal NPs to conduct photocatalysis under ambient conditions and reach an incredible conversion and selectivity, which provides valuable protocols for designing efficient photocatalysts to drive chemical transformations with light. For example, Xiao et al. describe an Au-Pd alloy photocatalytic system that catalyzes five cross-coupling reactions under mild conditions, including Stille, Hiyama, Sonogashira, Ullmann C−C couplings, and the Buchwald−Hartwig amination.[63] The temperatures of these reactions are slightly above room temperature, and the efficiency of these photocatalysts relies on the wavelength and intensity of the incident light. Towards the mechanism, Au-Pd alloy can strongly absorb incident light, where the conduction electrons on the Pd surfaces gain energy. According to density functional theory calculation, the energized electrons transfer from the NP surface to the absorbed reactant molecules, which activates the reactants. As the temperature rises, the reaction rates can be accelerated, and with the wavelength of the incident light goes towards UV range, some reactions with the chlorobenzene substrate can be driven. These discovery drives the exploration of new catalytic system to make chemical transformations happen under mild conditions.

2.3 TRANSFORMATION FROM BIOMASS TOWARDS VALUE-ADDED FINE CHEMICALS

2.3.1 Biomass-derived HMF

Continuously growing demands for energy, chemicals, and materials force humans to explore more renewable and sustainable feedstocks instead of petrochemicals from fossil fuels.[64, 65] lignocellulosic biomass (LCB) has a wide distribution globally with abundant reserves, making it an excellent potential to explore bio-based chemicals.[66] LCB initially includes lignin (20–30%) cellulose (40–50%), hemicelluloses (20–40%), and other trace components like protein and silica.[67] Cellulose can be converted into sugars or phenol through depolymerization and then transformed into monomers such

as ethylene, HMF, lactic acid (LA), etc.[12] Among these monomers, HMF is a top value-added bio-mass derived material because its derivatives (2,5-furandicarboxylic acid, 2,5-diformylfuran, furfuryl alcohol, and dimethylfuran) serve as building blocks in various fields, like pharmaceuticals, bio-fuels and polymers.[68] It is a white low-melting solid which is highly soluble in both water and organic solvents.

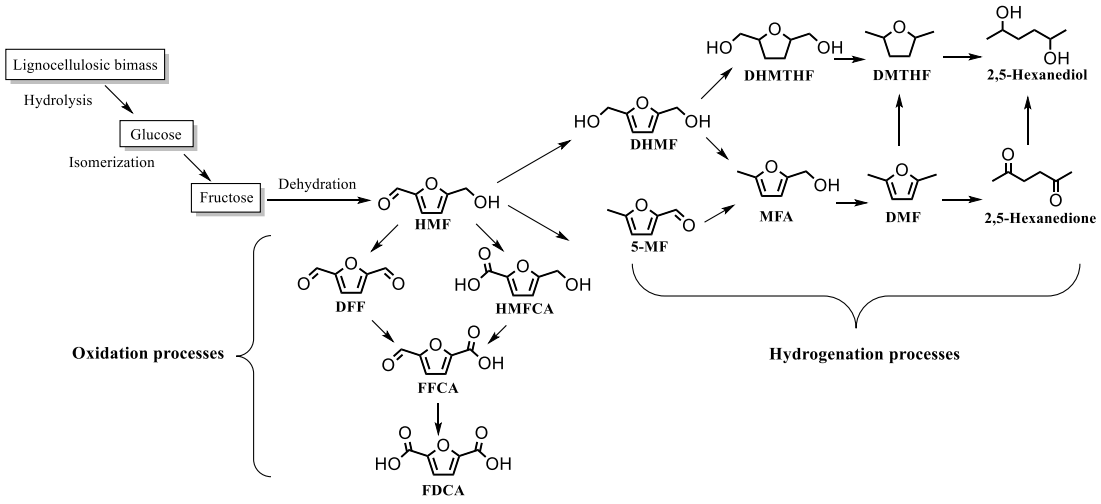

Figure 9 The possible pathways of high value-added chemicals from biomass.

One of the degradation products, furan-2,5-dicarboxylic acid (FDCA) has been suggested as an important renewable building block because it can replace terephthalic acid (PTA) in the production of polyesters and other current polymers containing aromatic moiety and has the advantage of being renewable. Industrial polymerization of terephthalic acid with ethylene glycol yields poly(ethylene terephthalate) (PET), which is produced at a rate of 50 million tons annually.[69] To compete as a renewable alternative to PET, an FDCA-based polymer must meet the same high standards of stability, mechanical strength, color, transparency, and gas barrier properties.

2.3.2 Oxidation of HMF to FDCA

Both homogeneous and heterogeneous catalytic synthesis of FDCA from HMF is a promising technique for FDCA production. However, due to the ease of separation and recycling of heterogeneous catalysts, homogeneous catalysts are less attractive.[70] Besides, homogeneous catalytic synthesis of FDCA from HMF usually has lower FDCA yield, and the problem of by-products to be overcome. Therefore, heterogeneous catalysis of FDCA generation has been a more promising technique for

both experimental attempts and potential commercialization compared to homogeneous catalysis. A variety of heterogeneous catalysts have been used in the oxidative production of FDCA from HMF.[71, 72] Air or pure oxygen are usually used as oxidizing agents during oxidation; hydrogen peroxide (H_2O_2) and potassium permanganate (KMnO4) are also used, however, molecular oxygen is preferred by researchers due to its higher oxidation potential, eco-friendly impact, and low cost. As well as platinum (Pt), gold (Au), ruthenium (Ru) and palladium (Pd), several metal supported heterogeneous catalysts have been developed and applied to HMF oxidation and FDCA with good catalytic activity, recyclability, and stability.[73, 74] Most of the heterogeneous catalysis scheme in FDCA research currently consists of noble metal supported on oxides.

Currently, HMF is selectively oxidized to FDCA over noble metal catalysts at elevated temperatures (80−150 °C). The disadvantages of these thermal catalytic oxidation processes are high catalyst costs, high energy consumption (due to high reaction temperatures), high oxygen pressures, and excessive base requirements, which impede industrial applications. Therefore, it is important to develop routes for selective oxidation of HMF into FDCA under mild conditions. The recent work on HMF oxidation to FDCA has been summarised in Table 1 with both thermo-assisted and photo-assisted reactions. These findings are HMF oxidation to FDCA using supported single metal NPs, like Au, Pd, Ru, Pt, and supported bimetallic NPs, such as Au-Pd, Au-Pt, etc.

2.4 SUMMARY AND IMPLICATIONS

According to the studies so far, the thermal reaction has thoroughly investigated the oxidation of HMF to FDCA. However, most of them have harsh reaction conditions, like high temperature and high pressure of oxidant gas, making them an obstacle to applying HMF oxidation in industry. On the other hand, the photo driven HMF oxidation to FDCA based on metal NPs is still worth exploring. This project starts by simplifying the reactions to mild conditions and utilizing solar energy to drive it More environmentally friendly.

Table 1 Recent heterogeneous catalytic synthesis of FDCA from HMF based on supported metal catalysts

Catalyst	Light or Thermo	Solvent	Base	Oxidant	Temperature (°C)	HMF conversion (%)	FDCA yield (%)	Ref.
Au/CeO_2	Thermo	H_2O	NaOH	1 MPa air	130	96	100	[75]
Au/Al_2O_3	Thermo	H_2O	NaOH	1 MPa O_2	70	100	99	[76]
Pd/PVP	Thermo	H_2O	NaOH	0.1 MPa O_2	90	>99	90	[77]
Pd/HT	Thermo	H_2O	--	0.1 MPa O_2	100	>99	>99	[78]
Ru/ZrO_2	Thermo	H_2O	--	1 MPa O_2	120	71	100	[79]
Ru/C	Thermo	H_2O	NaOH	0.2 MPa O_2	120	69	100	[80]
Pt/C	Thermo	H_2O	$NaHCO_3$	1 MPa O_2	110	99	99	[81]
Pt/ ZrO_2	Thermo	H_2O	Na_2CO_3	0.1 MPa O_2	75	100	94	[82]
Pt-Bi/ZrO_2	Thermo	H_2O	Na_2CO_3	4 MPa air	100	99	97	[83]
Pt–Bi/C	Thermo	H_2O	Na_2CO_3	4 MPa air	100	100	>99	[84]
AuPd/pBNxC	Thermo	H_2O	Na_2CO_3	0.3 MPa O_2	100	100	98	[85]
AuPd/AC	Thermo	H_2O	NaOH	0.3 MPa O_2	60	99	95	[86]
AuPt/AC	Thermo	H_2O	NaOH	0.3 MPa O_2	60	99	94	[86]
AuPd/HT	Thermo	H_2O	NaOH	0.1 MPa O_2	60	100	81	[87]
AuPd/TiO_2	Thermo	H_2O	NaOH	1 MPa O_2	70	100	90	[88]
CoPz/g-C_3N_4	Visible light	$Na_2B_4O_7$	--	1 bar air	RT	99	97	[89]
Ni/CdS	Blue LED	H_2O	--	--	RT	100	100	[90]

Chapter 3: Materials and Methods

3.1 MATERIALS

The chemicals were purchased from commercial suppliers and used as provided。 Cerium (III) nitrate hexahydrate (Sigma-Aldrich, $Ce(NO_3)_3 \cdot 6H_2O$, 99% trace metals basis), sodium borohydride (Aladdin, Shanghai, $NaBH_4$, ≥98.0%), silver nitrate (Sigma-Aldrich, $AgNO_3$, ≥99.0%), Palladium(II) chloride (Sigma-Aldrich, $PdCl_2$, 99%), 5-hydroxymethyl furfural (Sigma-Aldrich, >99%), Ethanol (Ajax Finechem, 99.5%). The water used in all the experiments was prepared through an ultra-purification system.

3.2 CATALYST PREPARATION

3.2.1 Preparation of CeO_2 fiber

The CeO_2 support was prepared via hydrothermal treatment. In a typical synthesis, a mixture of Ce $(NO_3)_3 \cdot 6H_2O$ (1.302 g) in deionized water (7.5 ml) and NaOH pellets (14.4 g) in deionized water (52.5 ml) was transferred in a stainless autoclave with a poly (tetrafluoroethylene) (PTFE) liner and was maintained at 100 ℃ for 24 h. After cooling the solution to room temperature, the solid was recovered from the autoclaved mixture and washed several times with water and ethanol. Finally, the product was obtained after being dried at 60 ℃ for one day.

3.2.2 Preparation of supported silver and palladium NPs photocatalysts

Two aqueous solutions of $AgNO_3$ and Na_2PdCl_4 were reduced one by one onto CeO_2 nanofiber, where the wt% of Ag and Pd takes up 3 wt% in total. For example, $Ag_{2.5}/CeO_2$ was firstly prepared by reducing silver nitrate aqueous solution (0.01 M, 11.95 ml) onto CeO_2 powder (500 mg) with fresh $NaBH_4$ aqueous solution (0.01 M, 12.5 ml). Then Na_2PdCl_4 aqueous solution (0.01 M, 2.42 ml) was reduced onto $Ag_{2.5}/CeO_2$ (200 mg) by $NaBH_4$ aqueous solution (0.15 M, 2.5 ml), leading to the target catalyst $Ag_{2.5}@Pd_{0.5}$.Where the volumes of $NaBH_4$ used was proportional to its wt%.

The Na_2PdCl_4 solution was prepared by dissolving four times equivalents of NaCl with $PdCl_2$ aqueous solution (0.01 M).

3.3 INSTRUMENTS

The particle size and morphology of the catalyst samples were characterized with a JEOL2100 transmission electron microscope (TEM) operating at 200 kV, equipped with a Gatan Orius SC1000 CCD camera. Nitrogen physisorption isotherms were measured at -196^{o}C on the Tristar II 3020. Before each measurement, the sample was degassed at 120^{o}C for 24 h under vacuum. An energy-dispersion X-ray (EDX) spectrometer (X-MAXN 80TLE, OXFORD Instruments) was equipped for elemental analysis. X-ray photoelectron spectroscopy (XPS) analysis was performed with a Kratos Axis Ultra photoelectron spectrometer using a mono Al Kα (1486.6 eV) source. The UV-visible diffuse reflectance spectra for the support and the photocatalysts were recorded using a Cary 5000 UV-VIS-NIR Spectrophotometer. X-ray diffraction (XRD) patterns of the samples were recorded on a Philips Analytical X'Pert PRO diffractometer using Cu Kα radiation (λ=1.5418 Å). The working power is 40 kV and 40 mA. The diffraction data were collected from 10 to 90^o with a resolution of 0.01^o (2θ). Attenuated total reflectance Fourier transform infrared (ATR-FTIR) spectra were collected by a Nicolet-5700 spectrometer in the wavenumber range between 4000 and 620 cm^{-1} at a resolution 4 cm^{-1}.

3.4 PHOTOCATALYTIC REACTIONS

The photocatalytic reactions were conducted in 20 mL Pyrex glass tubes, sealed with parafilm after added reactants and catalyst. The reaction mixture was stirred magnetically and irradiated under a Nelson halogen lamp (Philips Industries: 500W, wavelength in the range 400-750 nm) as the visible light source. The light intensity was measured by a digital power-reading device (Newport Optical Power Meter, model 1918-C) to be 0.5 W/ cm^2. Control reactions in the dark were carried out at the same temperature as the light reaction in an oil bath. The sample was diluted with water by 20 times and filtered through a Millipore filter (pore size 0.45 μm) at each time interval to remove the solid photocatalyst. The HMF oxidation products were quantified with commercial chemicals and analyzed by High-Performance Liquid

Chromatography (HPLC) 2014 coupled with LTQ Orbitrap Elite Mass Spectrometer (MS).

The temperatures were carefully controlled with an air cooler attached to the reaction apparatus. In the 60 °C reaction system, the temperature increased to the target value within around 4 minutes, recorded well with a thermal imaging camera (Figure 10).

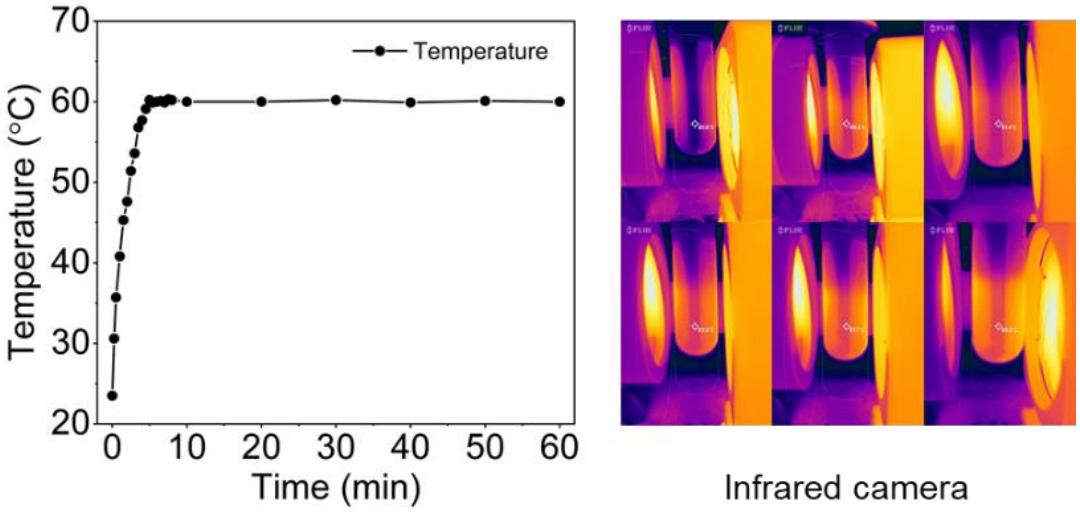

Figure 10 Temperature growth during the reaction catalyzed by $Ag_{2.5}@Pd_{0.5}$ photocatalyst, and the images were shot by FLIR thermal imaging camera.

3.5 FDCA YIELD AND SELECTIVITY CALCULATION

All the reactants, intermediates, and products, including HMF, HMFCA, FFCA (5-Formyl-2-furancarboxylic Acid), and FDCA, were dissolved into deionized water to make a 0.05/20M stock aqueous solution. Then all the stock was diluted into a series of standards solution, 0.0025/20 M, 0.005/20 M, 0.01/20 M, 0.02/20 M, 0.03/20 M, 0.04/20 M, 0.05/20 M to construct the calibration curve. After every reaction sample was diluted 20 times and measured by HPLC, the concentration of each reactant, intermediates, and product could be obtained according to the calibration curve.

$$\text{FDCA yield} = \frac{C_{FDCA}}{C_{HMF}} * 100\%$$

$$\text{FDCA selectivity} = \frac{C_{FDCA}}{C_{HMFCA}+C_{FFCA}+C_{FDCA}} * 100\%$$

Where C_{FDCA} represents the concentration of FDCA after reaction, as well as C_{HMFCA}, $+C_{FFCA}$, and C_{FDCA}.

3.6 ETHICS AND LIMITATIONS

The authors declare no ethics and limitations.

Chapter 4: Results and Discussion

4.1 CHARACTERIZATION OF THE CATALYSTS

The characteristic techniques include elemental analysis, Transmission electron microscopy (TEM), Scanning electron microscope (SEM), Energy-dispersive X-ray spectroscopy (EDS), and Ultraviolet-visible spectroscopy (UV-vis), X-ray diffraction (XRD), were used in this project to describe the structural information of the photocatalysts.

The transmission electron microscope (TEM) images of CeO_2 supported sample showed that $Ag_{2.5}@Pd_{0.5}$ cluster-shell NPs dispersed evenly on the supports. The cerium oxide support was synthesized as fine nanofibers shown in the spectra. The mean diameter of the NPs loaded on the support is approximately 7 nm (Figure 11a and b). According to the High-resolution X-ray photoelectron spectra (XPS) fittings (Table 2), the actual Ag:Pd ratios for $Ag_{2.5}@Pd_{0.5}/CeO_2$, $Ag_{2.0}@Pd_{1.0}/CeO_2$, $Ag_{1.5}@Pd_{1.5}/CeO_2$ are calculated to be 5:1.1, 2:0.99 and 1: 0.89. Apart from that, Energy-dispersive X-ray spectroscopy (SEM-EDX) mapping has also been conducted to verify the metal ratios (Figure 12), where the data indicated the ratios for these three samples are measured to be ,5:0.90, 2:1.13 and 1:0.99, the Ag/Pd ratios acceptably accord with expected values. Also, a TEM-EDX line scan has been conducted on the $Ag_{2.5}@Pd_{0.5}/CeO_2$ surface across a typical Ag@Pd NP, the line profile analysis (Figure 11d) and the information on the elemental composition indicate there are tiny palladium element dispersed outside the silver element. The line-scan spectrum proved the existence of the core-cluster structure for the Ag@Pd NP.

Overall, the TEM, SEM-EDX, and XPS elemental analysis results confirm the Ag@Pd NPs have been successfully loaded onto the surface of cerium oxide, and the ratios between Ag and Pd are expected as experimental calculations. Also, the surface structure is supposed to be a core-cluster structure

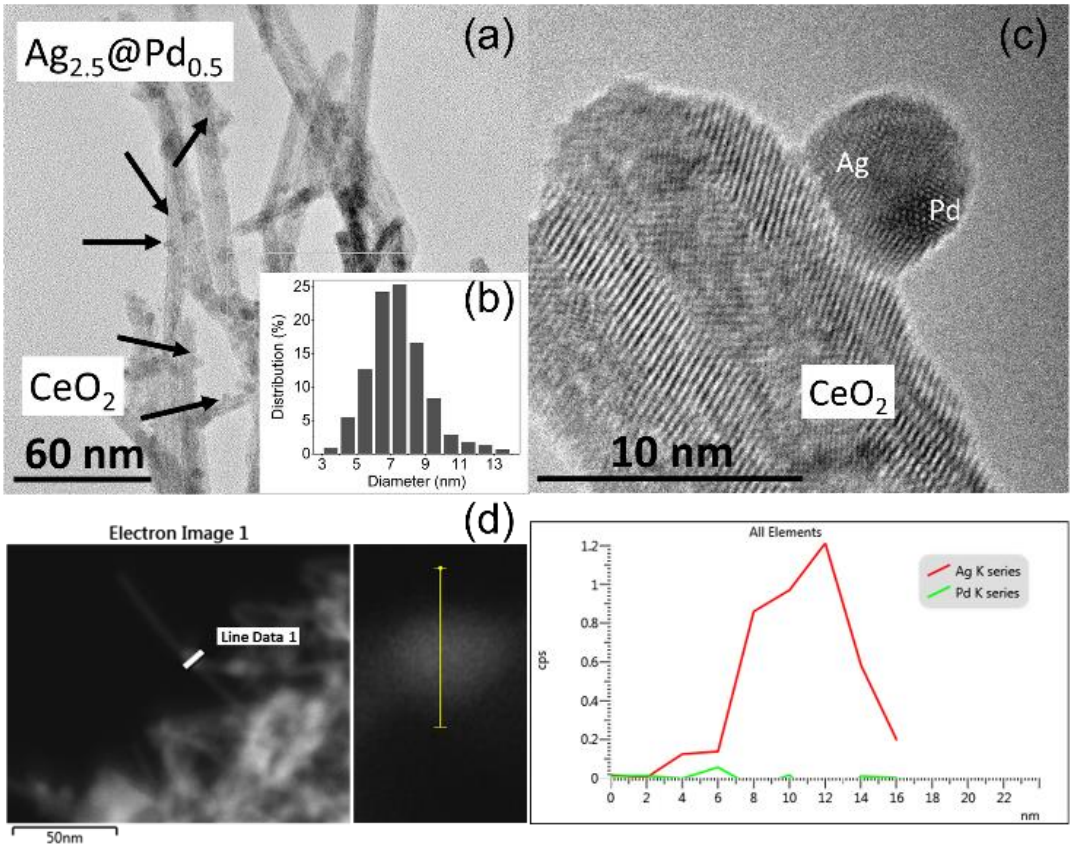

Figure 11 Catalyst characterization of CeO_2 supported $Ag_{2.5}@Pd_{0.5}$ photocatalyst. (a) Transmission electron microscopy (TEM) images. (b) Particle size distribution. (c) the lattice picture of the Ag@Pd NPs. (d) the line profile analysis of EDX spectra for a typical Ag@Pd NP and the elemental composition information.

Table 2 XPS elemental composition of the photocatalysts: $Ag_{2.5}@Pd_{0.5}/CeO_2$, $Ag_{2.0}@Pd_{1.0}/CeO_2$, and $Ag_{1.5}@Pd_{1.5}/CeO_2$.

Entry	Photocatalysts	Ag (%)	Pd (%)	Intended Ag: Pd	Actual Ag: Pd
1	$Ag_{2.5}@Pd_{0.5}$	82.03	17.97	5:1	5:1.10
2	$Ag_{2.0}@Pd_{1.0}$	66.69	33.31	2:1	2:0.99
3	$Ag_{1.5}@Pd_{1.5}$	53.02	46.98	1:1	1:0.89

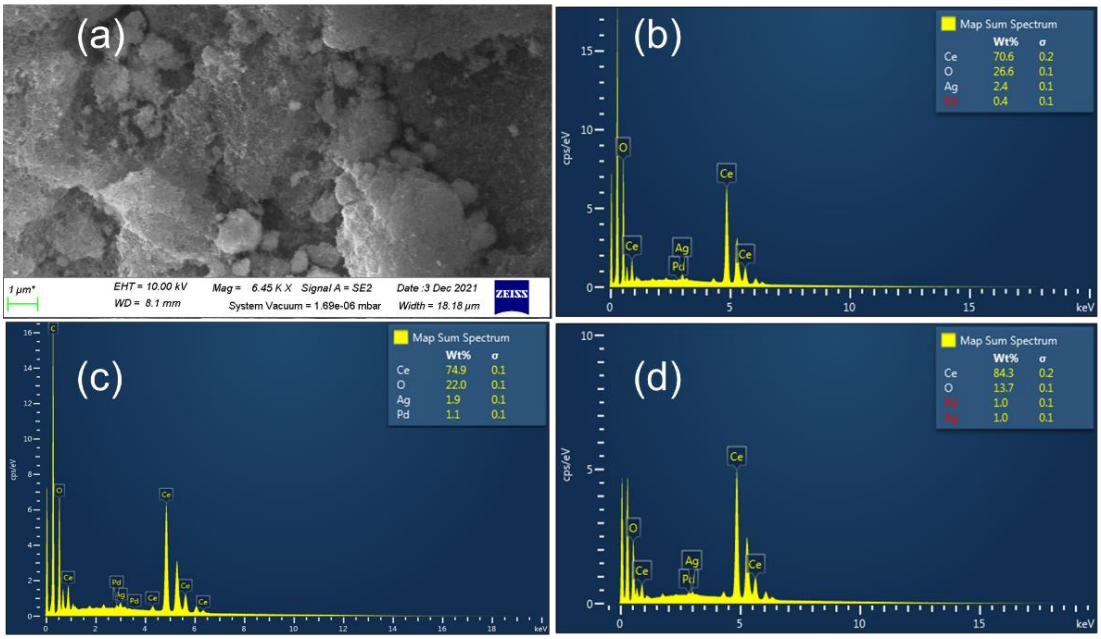

Figure 12 Scanning electron spectrum of (a) $Ag_{2.5}@Pd_{0.5}/CeO_2$; Energy-dispersive X-ray spectroscopy (SEM-EDX) mapping of (b) $Ag_{2.5}@Pd_{0.5}/CeO_2$, (c) $Ag_{2.0}@Pd_{1.0}/CeO_2$, and (c) $Ag_{1.5}@Pd_{1.5}/CeO_2$

The Powder X-ray diffraction (PXRD) results (Figure 13) have been conducted on a series of Ag@Pd samples with different Ag/Pd ratios, where the results show a slight change at around 38.6 degrees as the silver loading increases, which attribute to the Ag (111) diffraction.[91] However, no direct reflection peaks correspond to metallic palladium because its content is extremely low.

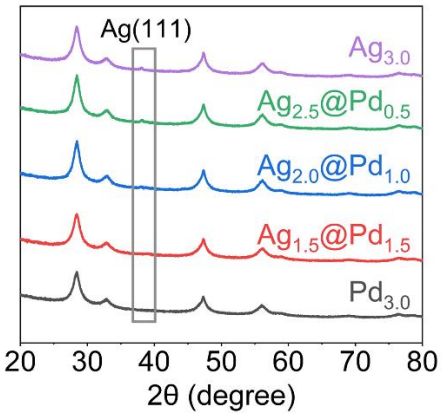

Figure 13 XRD patterns of catalysts with different Ag/Pd ratios.

To investigate more insight into the surface structure of the Ag@Pd photocatalysts, Figure 14 shows the XPS spectra of stacked data from samples

with various Ag/Pd ratios and mixed $Ag_{2.5}$ and $Pd_{0.5}/CeO_2$ samples. The mixed one has the same energy shift of Ag 3d and Pd 3d with pure $Ag_{3.0}$ and $Pd_{3.0}/CeO_2$. However, photocatalysts prepared by the method introduced in this study exhibit different changes relating to different Ag/Pd ratios. These results indicate that the Ag/Pd NP are ready to be a combination instead of separated in this system.

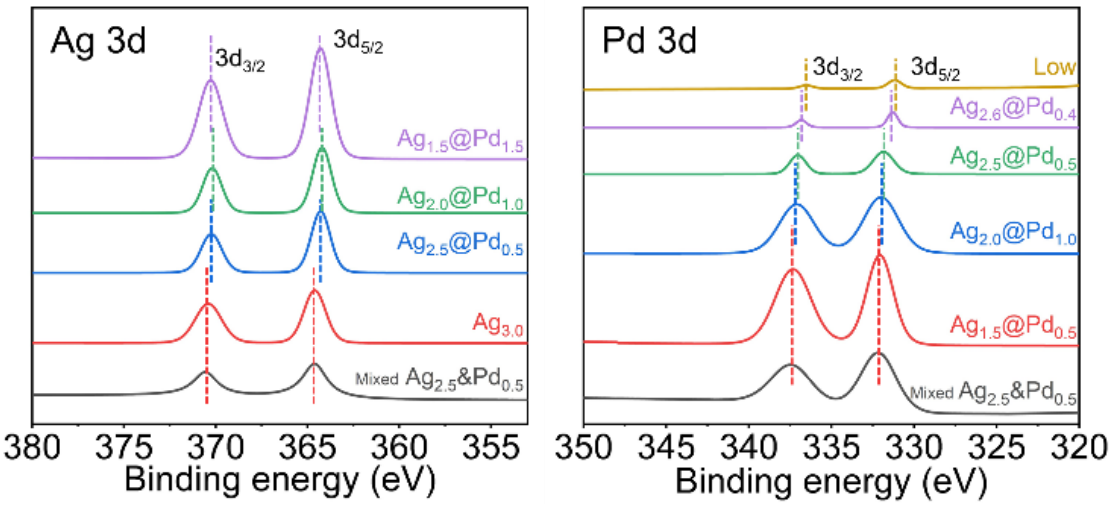

Figure 14 High resolution X-ray photoelectron spectra (XPS) for Ag $3d_{3/2}$, $3d_{5/2}$ and Pd $3d_{3/2}$, $3d_{5/2}$ of the photocatalysts: mixed $Ag_{2.5}$&$Pd_{0.5}/CeO_2$, $Ag_{3.0}/CeO_2$, $Ag_{2.5}@Pd_{0.5}/CeO_2$, $Ag_{2.0}@Pd_{1.0}/CeO_2$, $Ag_{1.5}@Pd_{1.5}/CeO_2$ and $Pd_{3.0}/CeO_2$.

Also, the UV-vis spectra comparison between the $Ag@Pd/CeO_2$ and the direct sum of Ag_3/CeO_2 and Pd_3/CeO_2 (Figure 15) shows a considerable difference. Therefore, it could be further confirmed that the Ag@Pd NPs are not separately dispersed on the cerium oxide but combined.

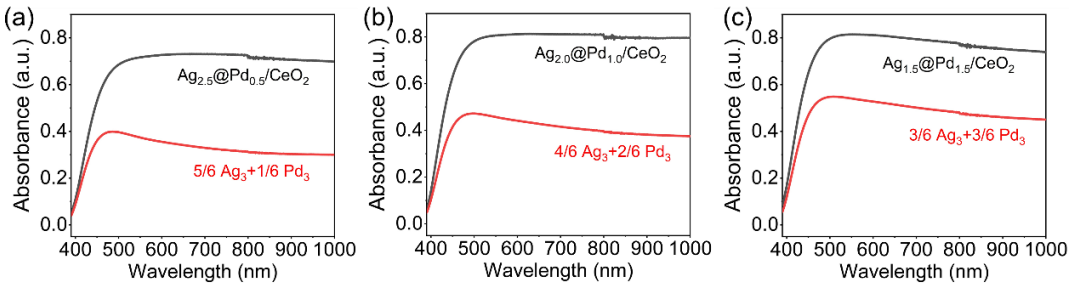

Figure 15 Characterization of the Ag@Pd photocatalyst. (a-c) Comparison of the UV-Visible spectra between the $Ag@Pd/CeO_2$ and direct sum of Ag_3/CeO_2 and Pd_3/CeO_2.

UV-vis spectra of the samples (Figure 16a) have provided much information on the light adsorption range. Firstly, it is evident from the spectra that the loading of silver

($Ag_{3.0}/CeO_2$) enhances the light absorbance ability of CeO_2. When the palladium is introduced onto the $Ag_{3.0}/CeO_2$ NPs, the absorbance of CeO_2 is further improved. As palladium content changes to 0.4 and 0.5 wt.%, the two high TON (Turnover number) points were observed, which agree with the slight peaks in the UV-vis spectra. The spectrum of single silver NPs supported on CeO_2 shows a broad peak at around 470 nm due to the LSPR absorption of the tiny silver particles.[92] The spectra of the Pd loaded catalysts strongly absorb visible light irradiation, proving the catalyst's photoactivity. While the Ag NPs LSPR absorption peaks towards a high wavelength, we can speculate that the Ag NPs interact and blend well with the Pd NPs.17 The metal NPs gather closely and aggregate, causing scattering, which leads to intense light absorption between 500-800 nm.[93] However, the support CeO_2 has broad adsorption between 300-500 nm,[91] the same as the CeO_2 supported catalysts. Therefore, the UV-vis spectra deducted CeO_2 were also constructed. Figure 16b shows that CeO_2 subtracted $Ag_{2.5}@Pd_{0.5}$ and $Ag_{2.6}@Pd_{0.4}$ exhibit a clear adsorption peak at around 510 nm, which agrees with the catalytic activity data (Table 4). This result proves that light adsorption will contribute to the catalytic activity.

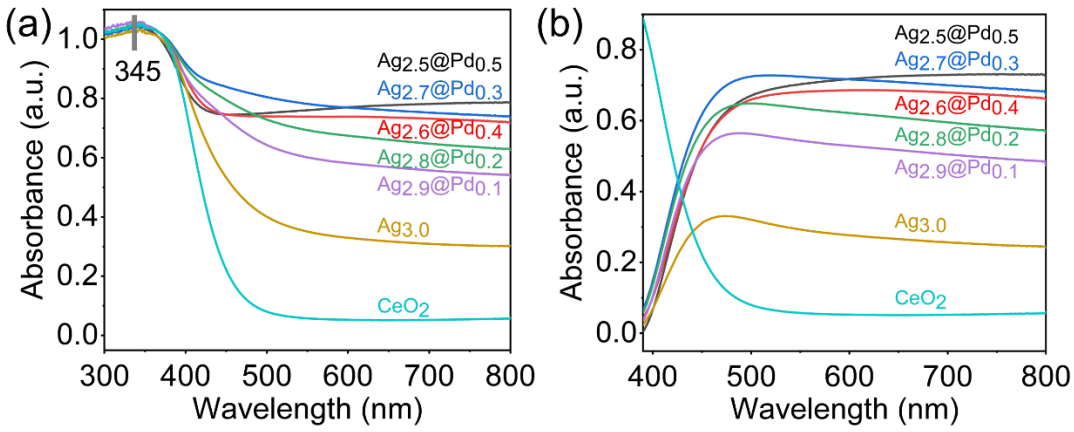

Figure 16 UV-visible diffuse reflectance spectra for the (a) support and the catalysts prepared by two reductions with different Ag/Pd ratios, (b) the spectra that have been deducted CeO_2.

Recent research has proved that the ensemble effect between the metal atoms and neighboring oxygen vacancies can promote oxygen transfer and drive reaction transformations.[94, 95] Besides, it has been claimed that even the oxygen vacancy itself can serve as the active site and enhance the adsorption of the reactants to promote the chemical reactions.[96, 97] Therefore, we explored the

concentration of the catalysts' surface oxygen vacancies and their chemical states. Figure 17 shows the XPS spectra and corresponding fittings of AgPd alloy and Ag@Pd catalysts, and Table 3 collected the Ce^{3+} concentrations. Pure CeO_2 has a Ce^{3+} concentration of 35.1%, $Ag_{1.5}@Pd_{1.5}/CeO_2$, $Ag_{2.0}@Pd_{1.0}/CeO_2$ have slight improvement to 37.2% and 39.1%, a peak value 41.4% was reached for $Ag_{2.5}@Pd_{0.5}/CeO_2$. Compared to alloy catalysts with the same AgPd ratios, Ag@Pd catalysts have different increase on $Ag_{1.5}Pd_{1.5}/CeO_2$, $Ag_{2.0}Pd_{1.0}/CeO_2$, $Ag_{2.5}Pd_{0.5}/CeO_2$, 9.2%, 4.6% and 5.6% respectively. As a result, we know that the preparing methods for Ag@Pd catalysts could create more oxygen vacancies to serve as the reaction sites than pure CeO_2 and AgPd alloy catalysts and then promote the chemical transformations.

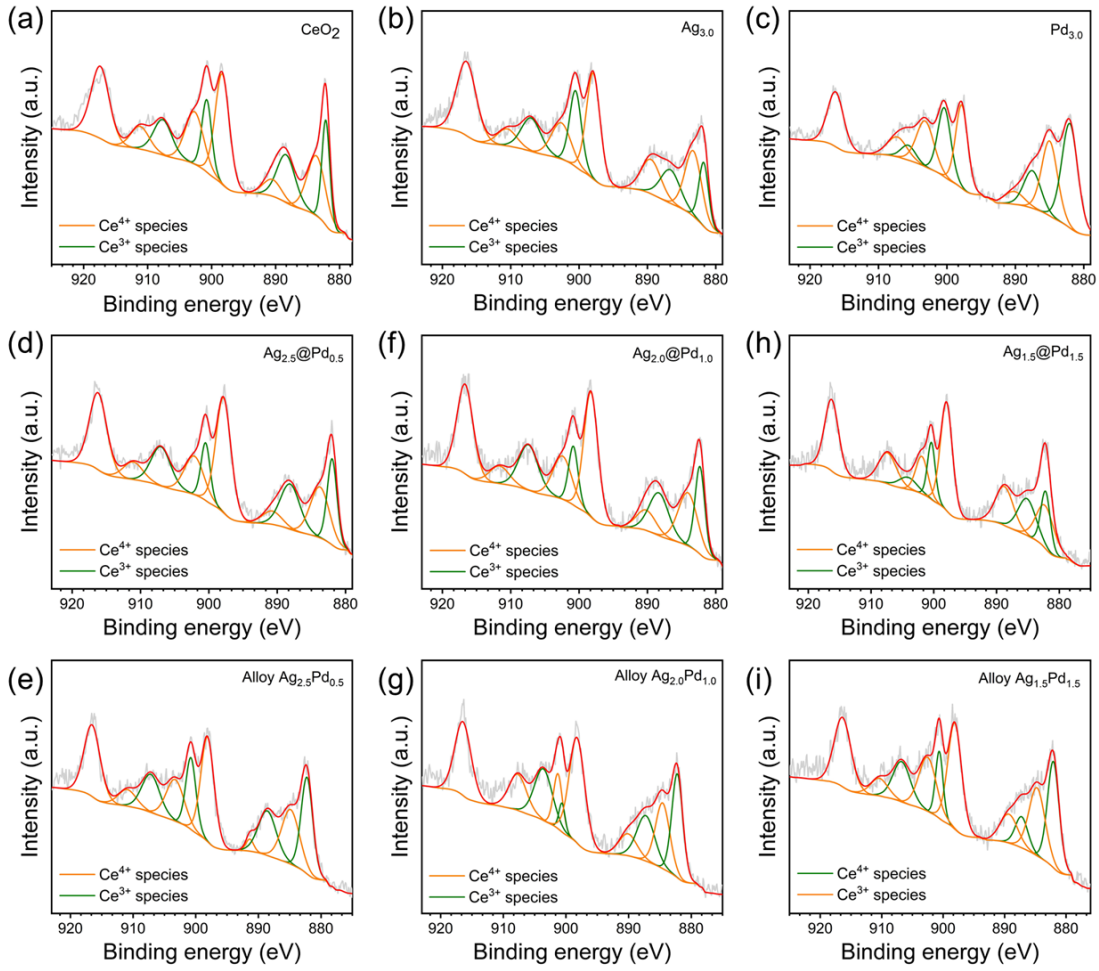

Figure 17 XPS spectra and corresponding fitting curves of Ce 3d in (a) CeO_2, (b) $Ag_{3.0}/CeO_2$, (c) $Pd_{3.0}/CeO_2$, (d) $Ag_{2.5}@Pd_{0.5}/CeO_2$, (e) $Ag_{2.5}Pd_{0.5}/CeO_2$, (f) $Ag_{2.0}@Pd_{1.0}/CeO_2$, (g) $Ag_{2.0}Pd_{1.0}/CeO_2$ (h) $Ag_{1.5}@Pd_{1.5}/CeO_2$, (i) $Ag_{1.5}Pd_{1.5}/CeO_2$. The green peaks are attributed to Ce^{3+} species (881.2, 884.9, 899.3 and 903.1 eV) while

the orange peaks are attributed to Ce^{4+} species (882.2, 888.2, 898.1, 900.7, 907.3 and 916.7 eV).[98]

Table 3 Proportions of Ce^{3+} and Ce^{4+} species in different catalysts.

Entry	Photocatalysts	Ce^{3+} species (%)	Ce^{4+} species (%)
1	CeO_2	35.1	64.9
2	$Ag_{3.0}/CeO_2$	33.0	67.0
3	$Pd_{3.0}/CeO_2$	43.2	56.8
4	$Ag_{2.5}@Pd_{0.5}/CeO_2$	41.4	58.6
5	$Ag_{2.5}Pd_{0.5}/CeO_2$	35.8	64.2
6	$Ag_{2.0}@Pd_{1.0}/CeO_2$	39.1	60.9
7	$Ag_{2.0}Pd_{1.0}/CeO_2$	34.5	65.5
8	$Ag_{1.5}@Pd_{1.5}/CeO_2$	37.2	62.8
9	$Ag_{1.5}Pd_{1.5}/CeO_2$	28.0	72.0

The proportion of Ce^{3+} species, P(Ce^{3+}) was calculated using the following equation, of which the areas are the fitting areas in XPS:

$$\text{Proportion } (Ce^{3+}) = \frac{\text{Area } (Ce^{3+})}{\text{Area } (Ce^{3+}) + \text{Area } (Ce^{4+})} \times 100\%$$

4.2 CATALYTIC PERFORMANCE OF HMF OXIDATION

Various catalysts with different palladium loadings were tested, and the results (Figure 16) showed the support itself and Ag/CeO_2 NPs did not contribute to the conversion. Pd/CeO_2 NPs only exhibited limited activity. Interestingly, $Ag_{2.5}@Pd_{0.5}/CeO_2$ had a high photoactivity on HMF oxidation to FDCA under the conditions listed, slightly higher than $Ag_{1.5}@Pd_{1.5}/CeO_2$. On the other hand, when comparing the turnover number of Pd elements (Figure 18), $Ag_{2.5}@Pd_{0.5}/CeO_2$ and $Ag_{2.6}@Pd_{0.4}/CeO_2$ show very high values than any different catalyst samples.

According to Figure 18a, when the Ag/Pd ratio reaches 2.5:0.5, an optimal FDCA yield is obtained, and the best light enhancement on the yield between light and dark reactions was received simultaneously. Figure 18b shows the TON number of the catalytic activity of the Pd element, where $Ag_{2.6}@Pd_{0.4}$ and $Ag_{2.5}@Pd_{0.5}$ have the highest value, indicating here palladium has the most efficient catalytic performance.

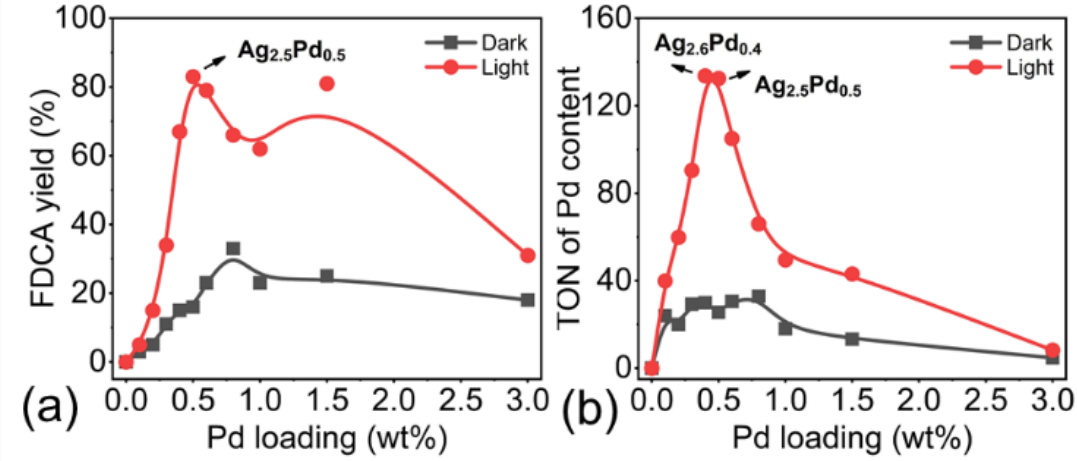

Figure 18 The reaction pathways for the catalytic oxidation of HMF to FDCA with molecular oxygen in water and the influence of palladium loading on (a) FDCA yield, and (b) TON (mol product/mol palladium loading). Reaction conditions without further noted: oxygen atmosphere at 60 °C using 0.15 mmol HMF, 0.4 mmol NaOH and 20 mg catalysts in 3 ml H_2O, the irradiation intensity was 1.0 W/cm^2.

Table 4 Optimization of the conditions for the oxidation of HMF to FDCA. The effect of palladium loading on HMF oxidation to FDCA using CeO2 supported Ag@Pd photocatalyst showed the catalytic performance under dark atmosphere in parenthesis.

Entry	Catalyst	FDCA yield (%)
1	Ag_3	0 (0)
2	$Ag_{2.9}@Pd_{0.1}$	5 (3)
3	$Ag_{2.8}@Pd_{0.2}$	13 (5)
4	$Ag_{2.7}@Pd_{0.3}$	34 (11)
5	$Ag_{2.6}@Pd_{0.4}$	67 (15)
6	$Ag_{2.5}@Pd_{0.5}$	83 (16)
7	$Ag_{2.4}@Pd_{0.6}$	79 (23)
8	$Ag_{2.2}@Pd_{0.8}$	66 (33)
9	$Ag_{2.5}$	0 (0)
10	$Pd_{0.5}$	10 (2)
11	$Pd_{3.0}$	36 (12)
12	CeO_2	0 (0)

The reactions above were conducted under an oxygen atmosphere at 60°C using 0.15 mmol HMF, 0.4 mmol NaOH and 20 mg catalysts in 3 ml H_2O, the irradiation intensity was 0.5 W/cm^2 and the reaction time was 4 h.

We have also conducted a series of experiments to optimize the above conditions. At 60°C, when the light intensity decreases from 1.0 to 0.2 W/cm^2, the productivity of FDCA also drops to 49%. On the other hand, when increasing the light intensity to 1.6 W/cm^2, the FDCA yield was not growing anymore, which indicates the activity peak has already been reached. The data of the light contribution was graphed in Figure 19b. The FDCA yield dependence on the light intensity means that the oxidation of HMF to FDCA is driven by electron transfer over the Ag@Pd NPs, and it can be controlled by tuning the irradiation intensity.

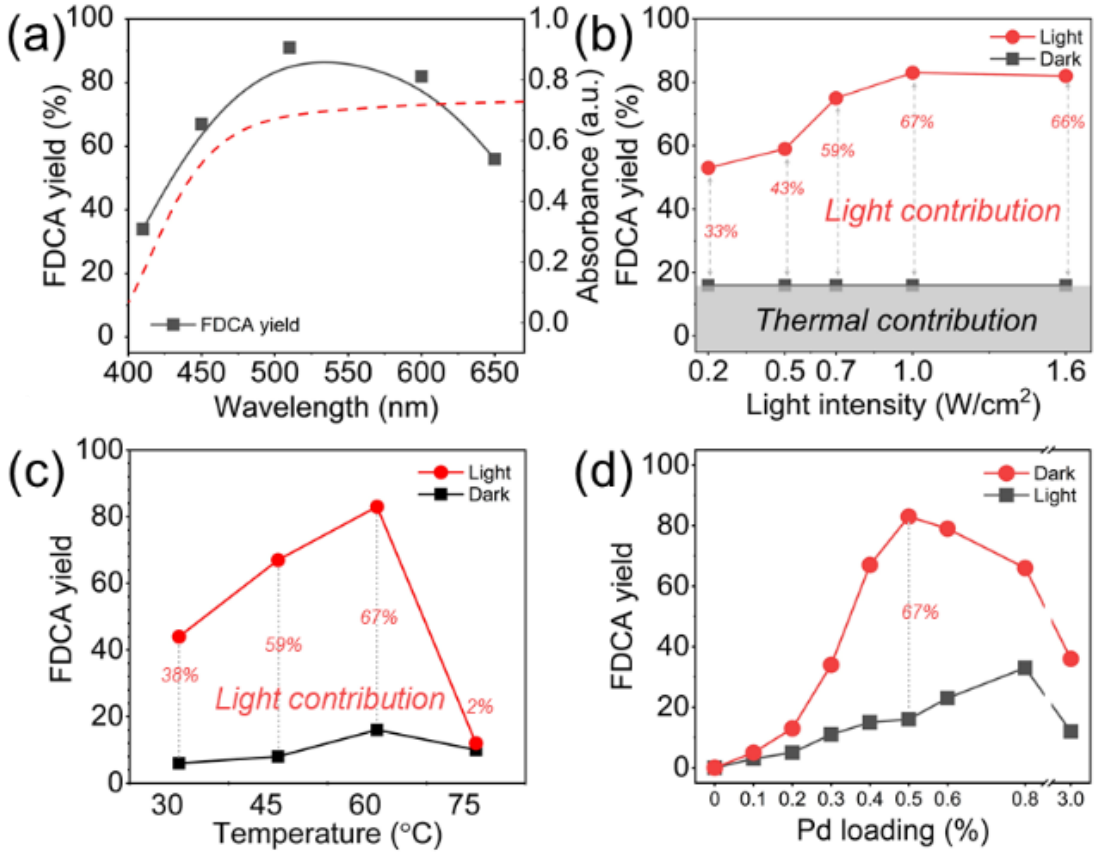

Figure 19 The influences of (a) light intensity, (b) temperature, (c) palladium loadings, (d) irradiation (0.5-0.6W/cm^2) wavelength on FDCA yield. Reaction conditions without further noted: oxygen atmosphere at 60°C using 0.15 mmol HMF, 0.4 mmol NaOH and 20 mg catalysts in 3 ml H_2O, the irradiation intensity was 1.0 W/cm^2.

Apart from the irradiation intensity, the dependence of FDCA yield on light wavelength was also explored. Because the reaction is driven by the energetic electrons excited by the incident light, so the reaction rate could be improved by

increasing the amount of the electrons. Here the number of electrons can be increased by tuning the irradiation wavelength and intensity.[99] An approach to telling if a reaction was driven by photo or thermal energy is the action spectrum, a one-to-one mapping between wavelength-dependent photocatalytic rate and the light extinction spectrum.[100,101] In this study, a series of experiments were conducted at 60°C under 0.5 W/cm^2 irradiation with different wavelengths, 410±5, 450±5, 500±5, 600±5 and 650±5 nm. The reaction rates were converted into apparent quantum yield (AQY%).[63] The AQY% values are calculated as follows: apparent quantum yield (AQY%) = $[(M_{light} - M_{dark})/Np] \times 100\%$, where M_{light} and M_{dark} are the molecules of products formed under irradiation and dark conditions, respectively, and N_p is the number of photons participated in the reaction. The action spectrum of the oxidation of HMF by Ag@Pd/CeO_2 is compared with its UV-vis absorption spectrum (Figure 19a). The action spectrum matches the catalyst's UV-visible spectrum (Figure 16b), which proves the Ag@Pd catalyst drive the HMF oxidation to FDCA by photo energy.

Temperature is also a critical factor in this photocatalytic reaction. It was found that light reactions were influenced significantly by temperature, and the FDCA yield nearly doubled from 30 to 60 ^oC (Figure 19c). When the temperature reached relatively high, the generation of by-products stopped the transformation from HMFCA to FFCA and FDCA, which resulted in the fall in FDCA yield. Compared to light reactions, the temperature change had little effect on the FDCA yield. The increasing temperature could increase the number of excited electrons, which can also get the energy from the LSPR effect.[63] As a result, the Ag@Pd photocatalyst can couple both thermal and photonic energy to promote the HMF oxidation to FDCA. Overall, the photocatalytic oxidation of HMF achieved a good FDCA yield (83%) under 1.0 W/cm^2 visible light and an excellent yield (91%) under 0.5 W/cm^2 green light.

Time-course reactions on pure Ag, Pd and $Ag_{2.5}$@$Pd_{0.5}$/CeO_2 (Figure 20) catalysts under dark, visible, and green light were conducted to investigate rate-determining steps for each catalyst. The data exhibits the excellent catalytic performance of the $Ag_{2.5}$@$Pd_{0.5}$ photocatalyst, avoiding mass loss and obtaining high FDCA yield under the same conditions compared to pure Ag and Pd

catalysts. Besides, $Ag_{2.5}@Pd_{0.5}$ significantly enhances the HMF conversion and transformation between HMFCA and FDCA compared to pure Pd catalysts.

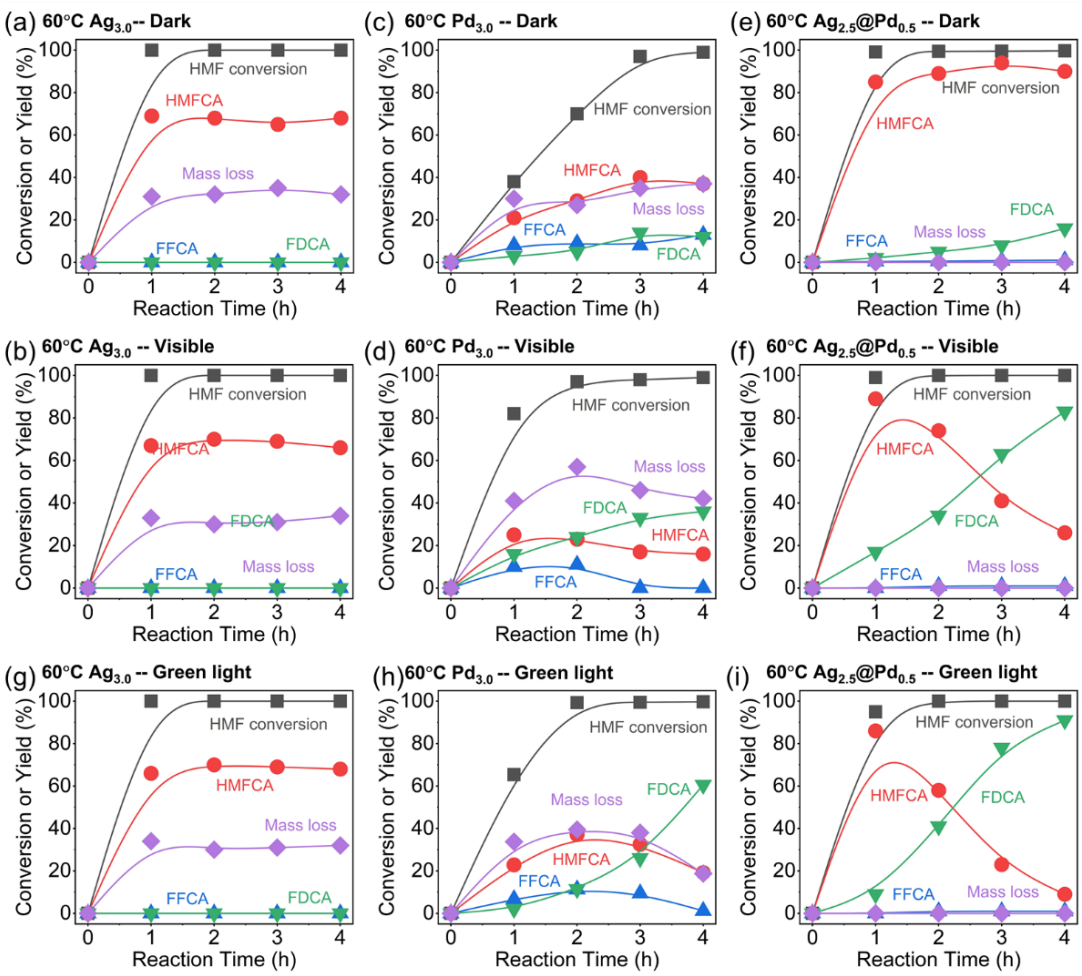

Figure 20 Time-course for the HMF oxidation reactions under dark and light irradiation over (a-b) $Ag_{3.0}/CeO_2$, (c-d) $Pd_{3.0}/CeO_2$, (e-f) $Ag_{2.5}@Pd_{0.5}/CeO_2$, (g-i) $Ag_{3.0}/CeO_2$, $Pd_{3.0}/CeO_2$ and $Ag_{2.5}@Pd_{0.5}/CeO_2$ under 0.5 W/cm^2 green light. The reactions without specially pointed out were conducted under an oxygen atmosphere at 60°C using 0.15 mmol HMF, 0.4 mmol NaOH and 20 mg catalysts in 3 ml H_2O, the irradiation intensity was 1.0 W/cm^2.

Apart from these factors, the influence of the support and reaction atmosphere has also been investigated. Commercial CeO_2, ZrO_2, TiO_2, SiO_2, and MgO have been used as the different supports compared with synthesized CeO_2 fibers, but little catalytical activity was found (Table 5). Compared to the oxygen atmosphere in this study, control experiments under air and argon (Table 6) exhibit no apparent activity. In conclusion, these data proved the unique

effectiveness of synthesized CeO_2 fiber and the necessity of oxygen in this reaction. Also, the recyclability of the $Ag_{2.5}@Pd_{0.5}/CeO_2$ photocatalyst has been tested. Figure 21 shows it exhibits stable catalytical activity after five runs, the conversion of HMF remains 100%, and the yields of FDCA fluctuate around 83% with ±5%. The recycle study confirms the Ag@Pd/CeO_2 catalysts are easily recoverable and stable in HMF oxidation reactions.

Table 5 The effect of different support on HMF oxidation to FDCA using supported Ag@Pd catalysts, the catalytic performance under dark atmosphere was shown in parenthesis.

Entry	Support	FDCA yield (%)
1	Synthesized CeO_2 fibre	83 (16)
2	Commercial CeO_2	6 (4)
3	ZrO_2	3 (2)
4	TiO_2	4 (2)
5	SiO_2	2 (1)
6	MgO	8 (25)

Table 6 The effect of reaction atmosphere on HMF oxidation to FDCA at 60 ^oC using CeO_2 supported Ag@Pd photocatalyst, the catalytic performance under dark atmosphere was shown in parenthesis

Entry	Atmosphere	FDCA yield (%)
1	O_2	83 (16)
2	Air	44 (7)
3	Ar	1 (1)

The reactions above were conducted under an oxygen atmosphere at 60°C using 0.15 mmol HMF, 0.4 mmol NaOH and 20 mg catalysts in 3 ml H_2O, the irradiation intensity was 0.5 W/cm^2 and the reaction time was 4 h.

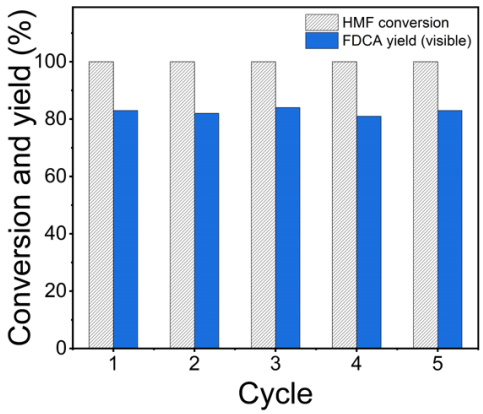

Figure 21 Recycle test of the $Ag_{2.5}@Pd_{0.5}/CeO_2$ catalyst in photocatalytic oxidation of HMF to FDCA. Reaction conditions: 0.15 mmol HMF, 0.4 mmol NaOH in 3 ml H_2O, oxygen atmosphere, 1.0 W/cm^2, reaction temperature 60^{o}C and reaction time 4h.

According to the study above, Figure 22 shows a possible mechanism for the HMF oxidation reaction. The silver NP strongly absorbs the light irradiation, causing the shift of the hot electrons. HMF molecules are absorbed onto the surface of the Ag@Pd to conduct the oxidation process. The activated hot electrons transfer from silver to Pd surface to contribute to oxidation, OH- is also involved in the transformation and finally released as H_2O. The products form and desorb the Pd NP surface into the aqueous solution.

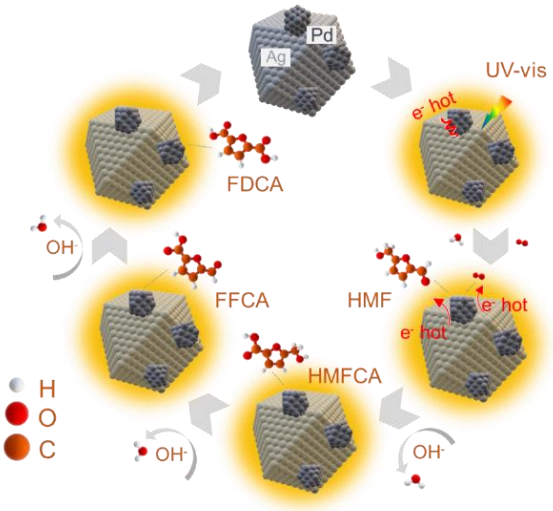

Figure 22 Proposed mechanism for the selective photocatalytic oxidation of HMF to FDCA over $Ag_{2.5}@Pd_{0.5}$ /CeO_2 surfaces

Chapter 5: Conclusions

This project introduced a new photocatalytic system of the Ag-Pd core-cluster supported on cerium oxide, which can efficiently catalyze the oxidation from HMF to FDCA with an excellent FDCA selectivity. The surface and spectroscopic properties of the catalysts have been analyzed by various characteristic techniques, including elemental analysis, ultraviolet-visible spectroscopy, transmission electron microscopy, scanning electron microscopy, X-ray diffraction, and energy-dispersive X-ray spectroscopy, X-ray photoelectron spectroscopy, and inductively coupled plasma optical emission spectrometry.

It has been proved that incident light irradiation can enhance the catalytic activity of active metal sites, giving an excellent yield of FDCA (91%) under green light, and a good yield (83%) under visible irradiation. The preponderance of this work is the utilization of solar energy to drive this chemical transformation, and the reaction conditions are very mild. Moreover, the palladium loading amount on the photocatalyst is extremely small, making this transformation economic to drive. The mechanism of this transformation was proposed. As silver NP absorbs light irradiation, it shifts electrons, which then conduct the oxidation process by absorbing HMF molecules onto the surface of Ag@Pd by absorbing light irradiation. In the silver oxidation reaction, a hot electron is transferred from the Pd surface to the Pd surface, OH- is involved, and finally, H_2O is released. In this reaction, products were generated and desorbed from the Pd NP surface into aqueous solution.

This finding may inspire further studies on novel metallic photocatalytic systems for various chemical transformations driven by green energy sources and cost-effective materials.

Bibliography

1. S. Peiris, J. McMurtrie and H.-Y. Zhu, *Catalysis Science & Technology*, 2016, **6**, 320-338.

2. Q. Xiao, S. Sarina, E. Jaatinen, J. Jia, D. P. Arnold, H. Liu and H. Zhu, *Green Chemistry*, 2014, **16**, 4272-4285.

3. J. Zhao, Z. Zheng, S. Bottle, A. Chou, S. Sarina and H. Zhu, *Chemical Communications*, 2013, **49**, 2676-2678.

4. S. Peiris, S. Sarina, C. Han, Q. Xiao and H.-Y. Zhu, *Dalton Transactions*, 2017, **46**, 10665-10672.

5. X. Chen, H. Y. Zhu, J. C. Zhao, Z. F. Zheng and X. P. Gao, *Angewandte Chemie*, 2008, **120**, 5433-5436.

6. A. Zaleska-Medynska, M. Marchelek, M. Diak and E. Grabowska, *Advances in colloid and interface science*, 2016, **229**, 80-107.

7. G. Sharma, V. K. Gupta, S. Agarwal, S. Bhogal, M. Naushad, A. Kumar and F. J. Stadler, *Journal of molecular liquids*, 2018, **260**, 342-350.

8. S. Shafiee and E. Topal, *Energy Policy*, 2009, **37**, 181-189.

9. G. W. Huber, S. Iborra and A. Corma, *Chemical Reviews*, 2006, **106**, 4044-4098.

10. M. Sajid, X. Zhao and D. Liu, *Green chemistry*, 2018, **20**, 5427-5453.

11. E. d. Jong, M. Dam, L. Sipos and G. Gruter, 2012.

12. A. A. Rosatella, S. P. Simeonov, R. F. M. Frade and C. A. M. Afonso, *Green Chemistry*, 2011, **13**, 754-793.

13. J. J. Bozell and G. R. Petersen, *Green Chemistry*, 2010, **12**, 539-554.

14. A. F. Sousa, C. Vilela, A. C. Fonseca, M. Matos, C. S. R. Freire, G.-J. M. Gruter, J. F. J. Coelho and A. J. D. Silvestre, *Polymer Chemistry*, 2015, **6**, 5961-5983.

15. A. Villa, M. Schiavoni, S. Campisi, G. M. Veith and L. Prati, *ChemSusChem*, 2013, **6**, 609-612.

16. B. Siyo, M. Schneider, J. Radnik, M.-M. Pohl, P. Langer and N. Steinfeldt, *Applied Catalysis A: General*, 2014, **478**, 107-116.

17. S. Sarina, H. Zhu, E. Jaatinen, Q. Xiao, H. Liu, J. Jia, C. Chen and J. Zhao, *Journal of the American Chemical Society*, 2013, **135**, 5793-5801.

18. Q. Xiao, S. Sarina, E. R. Waclawik, J. Jia, J. Chang, J. D. Riches, H. Wu, Z. Zheng and H. Zhu, *ACS Catalysis*, 2016, **6**, 1744-1753.

19. J. An, G. Sun and H. Xia, *ACS Sustainable Chemistry & Engineering*, 2019, **7**, 6696-6706.

20. E.-i. Negishi and L. Anastasia, *Chemical Reviews*, 2003, **103**, 1979-2018.

21. Y. Xin, L. Wu, L. Ge, C. Han, Y. Li and S. Fang, *Journal of Materials Chemistry A*, 2015, **3**, 8659-8666.

22. M. Aksoy, H. Kilic, B. Nişancı and Ö. Metin, *Inorganic Chemistry Frontiers*, 2021, **8**, 499-545.

23. Q. Yang, Q. Xu, S.-H. Yu and H.-L. Jiang, *Angewandte Chemie International Edition*, 2016, **55**, 3685-3689.

24. X. Meng, T. Wang, L. Liu, S. Ouyang, P. Li, H. Hu, T. Kako, H. Iwai, A. Tanaka and J. Ye, *Angewandte Chemie International Edition*, 2014, **53**, 11478-11482.

25. https://www.monex.com/investing-in-palladium/, *Journal*, 2022.

26. W. Partenheimer and Vladimir V. Grushin, *Advanced Synthesis & Catalysis*, 2001, **343**, 102-111.

27. J. Cai, H. Ma, J. Zhang, Q. Song, Z. Du, Y. Huang and J. Xu, *Chemistry – A European Journal*, 2013, **19**, 14215-14223.

28. P. V. Kamat, *The Journal of Physical Chemistry B*, 2002, **106**, 7729-7744.

29. S. Linic, P. Christopher, H. Xin and A. Marimuthu, *Accounts of chemical research*, 2013, **46**, 1890-1899.

30. Z. Zheng, B. Huang, X. Qin, X. Zhang, Y. Dai and M.-H. Whangbo, *Journal of Materials Chemistry*, 2011, **21**, 9079-9087.

31. S. Mubeen, J. Lee, N. Singh, S. Krämer, G. D. Stucky and M. Moskovits, *Nature Nanotechnology*, 2013, **8**, 247-251.

32. J. C. Scaiano, K. G. Stamplecoskie and G. L. Hallett-Tapley, *Chemical Communications*, 2012, **48**, 4798-4808.

33. X. Lu, M. Rycenga, S. E. Skrabalak, B. Wiley and Y. Xia, *Annual review of physical chemistry*, 2009, **60**, 167-192.

34. S. Linic, P. Christopher and D. B. Ingram, *Nature materials*, 2011, **10**, 911-921.

35. M. J. Kale, T. Avanesian and P. Christopher, *Acs Catalysis*, 2014, **4**, 116-128.

36. P. Christopher, H. Xin and S. Linic, *Nature chemistry*, 2011, **3**, 467-472.

37. J. A. Schuller, E. S. Barnard, W. Cai, Y. C. Jun, J. S. White and M. L. Brongersma, *Nature materials*, 2010, **9**, 193-204.

38. S. Linic, U. Aslam, C. Boerigter and M. Morabito, *Nature materials*, 2015, **14**, 567-576.

39. H. Petek and S. Ogawa, *Annual review of physical chemistry*, 2002, **53**, 507-531.

40. F. Le, D. W. Brandl, Y. A. Urzhumov, H. Wang, J. Kundu, N. J. Halas, J. Aizpurua and P. Nordlander, *ACS nano*, 2008, **2**, 707-718.

41. W. Hou and S. B. Cronin, *Advanced Functional Materials*, 2013, **23**, 1612-1619.

42. E. Kazuma, J. Jung, H. Ueba, M. Trenary and Y. Kim, *Science*, 2018, **360**, 521-526.

43. X. Lang, X. Chen and J. Zhao, *Chemical Society Reviews*, 2014, **43**, 473-486.

44. H. Li, Z. Bian, J. Zhu, Y. Huo, H. Li and Y. Lu, *Journal of the American Chemical Society*, 2007, **129**, 4538-4539.

45. L. Hang, Y. Zhao, H. Zhang, G. Liu, W. Cai, Y. Li and L. Qu, *Acta Materialia*, 2016, **105**, 59-67.

46. Y. Liu, Z. Liu, D. Huang, M. Cheng, G. Zeng, C. Lai, C. Zhang, C. Zhou, W. Wang and D. Jiang, *Coordination Chemistry Reviews*, 2019, **388**, 63-78.

47. C. Song, *Advances in Catalysis*, Elsevier Science & Technology, Saint Louis, UNITED STATES, 2017.

48. P. Munnik, P. E. de Jongh and K. P. de Jong, *Chemical Reviews*, 2015, **115**, 6687-6718.

49. C. Song, *Advances in Catalysis*, Elsevier Science, Saint Louis, 2016.

50. M. N. Kopylovich, A. P. C. Ribeiro, E. C. B. A. Alegria, N. M. R. Martins, L. M. D. R. S. Martins and A. J. L. Pombeiro, in *Advances in Organometallic Chemistry*, ed. P. J. Pérez, Academic Press, 2015, vol. 63, pp. 91-174.

51. S. Sarina, S. Bai, Y. Huang, C. Chen, J. Jia, E. Jaatinen, G. A. Ayoko, Z. Bao and H. Zhu, *Green Chemistry*, 2014, **16**, 331-341.

52. Y. Huang, C. Liu, M. Li, H. Li, Y. Li, R. Su and B. Zhang, *ACS Catalysis*, 2020, **10**, 3904-3910.

53. Y. Zhang, Q. Xiao, Y. Bao, Y. Zhang, S. Bottle, S. Sarina, B. Zhaorigetu and H. Zhu, *The Journal of Physical Chemistry C*, 2014, **118**, 19062-19069.

54. S. Benkhaya, S. M'rabet and A. El Harfi, *Inorganic Chemistry Communications*, 2020, **115**, 107891.

55. Z. Liu and M. Jiang, *Journal of Materials Chemistry*, 2007, **17**, 4249-4254.

56. B. Mondal and P. S. Mukherjee, *Journal of the American Chemical Society*, 2018, **140**, 12592-12601.

57. H. Zhu, X. Yuan, Q. Yao and J. Xie, *Nano Energy*, 2021, **88**, 106306.

58. S. Jana, F. He and R. M. Koenigs, *Organic Letters*, 2020, **22**, 4873-4877.

59. N. Miyaura and A. Suzuki, *Chemical Reviews*, 1995, **95**, 2457-2483.

60. S. E. Hooshmand, B. Heidari, R. Sedghi and R. S. Varma, *Green Chemistry*, 2019, **21**, 381-405.

61. Y. Meng, M. Wang and X. Jiang, *Angewandte Chemie*, 2020, **132**, 1362-1369.

62. X. Li, Z. Li and Y. W. Yang, *Advanced Materials*, 2018, **30**, 1800177.

63. Q. Xiao, S. Sarina, A. Bo, J. Jia, H. Liu, D. P. Arnold, Y. Huang, H. Wu and H. Zhu, *ACS Catalysis*, 2014, **4**, 1725-1734.

64. L. Ardemani, G. Cibin, A. J. Dent, M. A. Isaacs, G. Kyriakou, A. F. Lee, C. M. Parlett, S. A. Parry and K. Wilson, *Chemical science*, 2015, **6**, 4940-4945.

65. I. Delidovich, P. J. Hausoul, L. Deng, R. Pfützenreuter, M. Rose and R. Palkovits, *Chemical reviews*, 2016, **116**, 1540-1599.

66. J. Zhang, L. Lin and S. Liu, *Energy & fuels*, 2012, **26**, 4560-4567.

67. H. Kobayashi and A. Fukuoka, *Green Chemistry*, 2013, **15**, 1740-1763.

68. I. K. M. Yu and D. C. W. Tsang, *Bioresource Technology*, 2017, **238**, 716-732.

69. S. Pandey, M.-J. Dumont, V. Orsat and D. Rodrigue, *European Polymer Journal*, 2021, **160**, 110778.

70. M. Sajid, X. Zhao and D. Liu, *Green Chemistry*, 2018, **20**, 5427-5453.

71. Z. Zhang and K. Deng, *Acs Catalysis*, 2015, **5**, 6529-6544.

72. L. Hu, J. Xu, S. Zhou, A. He, X. Tang, L. Lin, J. Xu and Y. Zhao, *ACS Catalysis*, 2018, **8**, 2959-2980.

73. S. Xu, P. Zhou, Z. Zhang, C. Yang, B. Zhang, K. Deng, S. Bottle and H. Zhu, *Journal of the American Chemical Society*, 2017, **139**, 14775-14782.

74. C. Chen, X. Li, L. Wang, T. Liang, L. Wang, Y. Zhang and J. Zhang, *Acs Sustainable Chemistry & Engineering*, 2017, **5**, 11300-11306.

75. O. Casanova, S. Iborra and A. Corma, *ChemSusChem: Chemistry & Sustainability Energy & Materials*, 2009, **2**, 1138-1144.

76. C. Megías-Sayago, A. Lolli, S. Ivanova, S. Albonetti, F. Cavani and J. A. Odriozola, *Catalysis Today*, 2019, **333**, 169-175.

77. B. Siyo, M. Schneider, M.-M. Pohl, P. Langer and N. Steinfeldt, *Catalysis letters*, 2014, **144**, 498-506.

78. Y. Wang, K. Yu, D. Lei, W. Si, Y. Feng, L.-L. Lou and S. Liu, *ACS Sustainable Chemistry & Engineering*, 2016, **4**, 4752-4761.

79. C. M. Pichler, M. G. Al‐Shaal, D. Gu, H. Joshi, W. Ciptonugroho and F. Schüth, *ChemSusChem*, 2018, **11**, 2083-2090.

80. G. Yi, S. P. Teong and Y. Zhang, *Green chemistry*, 2016, **18**, 979-983.

81. H. Yu, K.-A. Kim, M. J. Kang, S. Y. Hwang and H. G. Cha, *ACS Sustainable Chemistry & Engineering*, 2019, **7**, 3742-3748.

82. R. Sahu and P. L. Dhepe, *Reaction Kinetics, Mechanisms and Catalysis*, 2014, **112**, 173-187.

83. H. Ait Rass, N. Essayem and M. Besson, *ChemSusChem*, 2015, **8**, 1206-1217.

84. H. A. Rass, N. Essayem and M. Besson, *Green chemistry*, 2013, **15**, 2240-2251.

85. W. Guan, Y. Zhang, Y. Chen, J. Wu, Y. Cao, Y. Wei and P. Huo, *Journal of Catalysis*, 2021, **396**, 40-53.

86. A. Villa, M. Schiavoni, S. Campisi, G. M. Veith and L. Prati, *ChemSusChem*, 2013, **6**, 609-612.

87. H. Xia, J. An, M. Hong, S. Xu, L. Zhang and S. Zuo, *Catalysis Today*, 2019, **319**, 113-120.

88. S. Cattaneo, D. Bonincontro, T. Bere, C. J. Kiely, G. J. Hutchings, N. Dimitratos and S. Albonetti, *ChemNanoMat*, 2020, **6**, 420-426.

89. S. Xu, P. Zhou, Z. Zhang, C. Yang, B. Zhang, K. Deng, S. Bottle and H. Zhu, *Journal of the American Chemical Society*, 2017, **139**, 14775-14782.

90. G. Han, Y.-H. Jin, R. A. Burgess, N. E. Dickenson, X.-M. Cao and Y. Sun, *Journal of the American Chemical Society*, 2017, **139**, 15584-15587.

91. S. Chang, M. Li, Q. Hua, L. Zhang, Y. Ma, B. Ye and W. Huang, *Journal of Catalysis*, 2012, **293**, 195-204.

92. M. M. Khan, S. A. Ansari, J.-H. Lee, M. O. Ansari, J. Lee and M. H. Cho, *Journal of colloid and interface science*, 2014, **431**, 255-263.

93. S. Sarina, H. Y. Zhu, Q. Xiao, E. Jaatinen, J. Jia, Y. Huang, Z. Zheng and H. Wu, *Angewandte Chemie*, 2014, **126**, 2979-2984.

94. L. Chen, Z. Qi, X. Peng, J.-L. Chen, C.-W. Pao, X. Zhang, C. Dun, M. Young, D. Prendergast and J. J. Urban, *Journal of the American Chemical Society*, 2021, **143**, 12074-12081.

95. K. Yu, L. L. Lou, S. Liu and W. Zhou, *Advanced Science*, 2020, **7**, 1901970.

96. B. Liu, C. Li, G. Zhang, X. Yao, S. S. Chuang and Z. Li, *ACS Catalysis*, 2018, **8**, 10446-10456.

97. G. Zhou, H. Liu, K. Cui, A. Jia, G. Hu, Z. Jiao, Y. Liu and X. Zhang, *Applied Surface Science*, 2016, **383**, 248-252.

98. E. Bêche, P. Charvin, D. Perarnau, S. Abanades and G. Flamant, *Surface and Interface Analysis: An International Journal devoted to the development and application of techniques for the analysis of surfaces, interfaces and thin films*, 2008, **40**, 264-267.

99. M. A. García, *Journal of Physics D: Applied Physics*, 2011, **44**, 283001.

100. A. Tanaka, S. Sakaguchi, K. Hashimoto and H. Kominami, *Acs Catalysis*, 2013, **3**, 79-85.

101. E. Kowalska, R. Abe and B. Ohtani, *Chemical Communications*, 2009, 241-243.